THE ASTROPHYSICAL JOURNAL, 288:94–116, 1985 January 1

BROAD EMISSION FEATURES IN QSOs AND ACTIVE GALACTIC NUCLEI. II. NEW OBSERVATIONS AND THEORY OF Fe II AND H I EMISSION

BEVERLEY J. WILLS,[1] HAGAI NETZER,[2] AND D. WILLS
Department of Astronomy and McDonald Observatory, University of Texas at Austin
Received 1984 April 26; accepted 1984 July 17

ABSTRACT

We have observed seven low and intermediate redshift QSOs and calculated new models to fit all spectral features between rest wavelengths of about 1800 and 5500 Å. A grid of photoionization models has been used to calculate the strengths of the Balmer continuum and of more than 45 Balmer lines. We have also extended our previous calculations of the Fe^+ atom and have included about 3000 Fe II lines in our models. We conclude: (1) High-order Balmer lines, the Balmer continuum, and numerous Fe II lines form an apparent continuum, in excess of the underlying central source continuum, from 1850 to 5000 Å. The underlying component can be fitted by a single flat power-law continuum. However, in most cases there is a rise in this underlying continuum at wavelengths longer than about Hβ. (2) Merging of high-order Balmer lines with the Balmer continuum nicely explains the smooth rise between about 4000 and 3700 Å. The observed Balmer continuum flux is about 5–10 times stronger than Hβ—stronger than that predicted by most photoionization models. The Balmer continuum shape can be fitted both by models with high temperature ($\sim$15,000 K) and low optical depth, and by models with low temperature ($\sim$10,000 K) and high optical depth. (3) Fe II lines provide $\gtrsim$50% of the excess energy between 2000 and 4000 Å. Fe II is the single largest contributor to the emission-line spectrum. In particular, I(Fe II)/I(Lyα) $\approx$ 1–2, and there is clearly a "Lyα/Fe II problem." (4) All objects in our sample have strong ultraviolet Fe II lines, regardless of the strength of the optical Fe II lines. The intensity ratio of UV to optical Fe II emission ranges from 4 to 12. (5) The observed ratio I[Fe II(UV)]/I[Mg II λ2798] suggests an overabundance of iron by a factor of $\sim$3 relative to magnesium and probably also to hydrogen. (6) Conventional dustless standard photoionization models cannot explain the strength of the observed Fe II lines, and an additional high-density component may be required. Small amounts of intrinsic reddening help to explain both the total Fe II flux and the observed ratio of ultraviolet to optical Fe II emission.

Subject headings: line formation — quasars — spectrophotometry

I. INTRODUCTION

Strong, broad lines observed in the spectra of QSOs and active galactic nuclei have been quite successfully explained in terms of photoionization of many dense ($\sim 10^{10}$ cm^{-3}) cloudlets having approximately cosmic abundances and partially covering a central source of power-law continuum radiation (Davidson and Netzer 1979 and references therein; Kwan and Krolik 1981). Many observational studies have concentrated on the low- and high-redshift objects. More recently attention has been paid to the intermediate-redshift QSOs, where the rest wavelengths (1500–6000 Å), accessible from the ground, include features caused by blended Fe II multiplets and the Balmer continuum (e.g., Wills, Netzer, and Wills 1980; Wills *et al.* 1980; Gaskell 1981; Grandi 1981, 1982; Malkan 1983; Malkan and Sargent 1982; Bergeron and Kunth 1984; Oke, Shields, and Korycansky 1984). Although this region is accessible for low-redshift QSOs and active galaxies using the *International Ultraviolet Explorer* (*IUE*), the spectra are not generally of sufficient quality to study the weaker emission features.

This is the second paper in a series in which we study Fe II lines, the Balmer continuum, and the Balmer lines, and improve significantly on earlier work by reproducing these features and the observed strengths of other broad emission lines, in models that include all important processes expected in the photoionized clouds of QSOs. Gas clouds are distributed symmetrically about a central ionizing continuum source, and we assume no shadowing of one cloud by another (small covering factor). Previous observational and theoretical studies of Fe II emission were summarized by Netzer and Wills (1983, hereafter Paper I), where we presented new calculations for Fe II lines and demonstrated that processes not considered before, mainly fluorescence due to wavelength coincidences of different Fe II lines, are very important. We also described a way to calculate the intensities of thousands of Fe II lines, and to relate them to photoionization calculations.

In this second paper we apply the results of Paper I to new, well-calibrated, high-quality spectra of seven low- and intermediate-redshift QSOs. Comparison of synthetic spectra with observations has led us to investigate the relation between the Fe II spectrum and other lines, in particular Mg II λ2798 and the hydrogen Lyα and Balmer lines. Some improvements in the previous calculations of Fe II, Mg II, and the Balmer lines and continuum are described in § II, and later used, together with the results of Paper I, to deduce the physical conditions in the broad emission-line clouds. The new observations are presented in § III, and details of instrumentation, observing, and data reduction are given in the Appendix. In § IV we describe our spectrum-fitting procedure and compare models with observed spectra to derive strengths of Fe II emission and other features, showing that Fe II emission is much stronger than

[1] Guest Investigator of the *IUE* Observatory, operated by Goddard Space Flight Center, National Aeronautics and Space Administration.
[2] On leave from Department of Physics and Astronomy and the Wise Observatory, Tel-Aviv University.

previously imagined. Then in § V we discuss the consequences for the physical conditions in the broad-emission-line clouds of QSOs and active galactic nuclei.

We want to remind the reader of several terms from Paper I that will be used again. We divide Fe II emission lines into three wavelength bands: Fe II(UV), comprising all lines between 2000 and 3000 Å; Fe II(3000–3500 Å); and Fe II(opt) (all lines with 3500 Å $< \lambda <$ 6000 Å). The term "line fluorescence" refers to absorption of one Fe II line photon by Fe^+ in a different transition. Fe II line optical depths are usually represented by the optical depth, $\tau(2343)$, in one resonance line of multiplet UV3. This optical depth depends, among other things, on the turbulent motion, V_t, in the cloud. We specify V_t only if it is larger than thermal velocities, and assume random motion. We use τ(Bac) and I(Bac) to indicate the optical depth at 3646 Å, and the total emission in the hydrogen Balmer continuum. The term "Balmer continuum destruction" is used to describe the process by which Fe II or Mg II λ2798 line photons are absorbed by the hydrogen $n = 2$ level.

II. CALCULATIONS

a) Fe II *and* Mg II *Lines*

Our assumptions and methods for calculating the level populations and line transfer of Fe II are outlined in Paper I. There are four minor changes that we should comment on. (1) We have added many more odd-parity terms to our model of the Fe^+ atom. Now it includes all levels up to 10.4 eV (1084 multiplets containing 3407 lines). Almost all lines from Kurucz's (1981) list with 1200 Å $< \lambda <$ 9000 Å and $\log(gf) > -5.5$ are included. (2) We have added many wavelength coincidences found by a more systematic search of all lines in Kurucz's list (now a total of approximately 300 line pairs with separation of less than 7.5 km s^{-1}; see Paper I for justification of this value). Both these changes have only small effects on the results. (3) We have considered the possibility that large turbulent motion inside a QSO cloud causes more line overlapping and fluorescence. Such a situation may arise if internal pressure (e.g., the result of scattering of Lyα and other line photons; see Ferland and Elitzur 1984) is important. Increasing the fluorescence criterion from 7.5 km s^{-1} (appropriate for thermal motion and $V_t = 0$) to 15 km s^{-1} (i.e., $V_t \geq 3$ km s^{-1}) roughly doubles the number of line coincidences (640),[3] and this changes the intensities of a few individual multiplets. However, the intensity over intervals of several hundred angstroms does not change very significantly. Increasing the line fluorescence tends to increase the total strengths of the ultraviolet relative to the optical lines, since it provides other escape routes for the highly trapped ultraviolet lines (see Paper I). These differences are not large enough to justify a full discussion of the physical situation that may result through such increase of the random motion. (4) We have modified the escape probability formula used, to take into account the smaller number of scatterings at high optical depth expected for interlocked lines (e.g., Puetter and Hubbard 1983). The resulting changes in line intensities are very small.

Destruction of Fe II line photons as a result of absorption by the hydrogen $n = 2$ level was discussed in Paper I. We have reevaluated this process because it strongly influences the Fe II ultraviolet-to-optical line ratio. This destruction can be separated into two components (see also Paper I and Kwan 1984): (1) "local" destruction, resulting in reduction of level populations in the small region in physical space where most scattering takes place, and (2) "nonlocal" destruction of the escaping photons, in which only a few scatterings occur, but the increase in path length traveled by the photons is significant. Unfortunately, the available Monte Carlo calculations (Ferland and Netzer 1979; Bonilha *et al.* 1979) do not give the location of line absorption and cannot be used to separate the local from the nonlocal destruction. This is a potential problem, since the two cause opposite changes in the relative strengths of the ultraviolet Fe II lines. Local destruction decreases the level populations in the region where the Balmer opacity is largest. This is also the region where most of the optical Fe II line emission originates, so the intensity ratio Fe II(UV)/Fe II(opt) tends to increase. Nonlocal destruction is important only for line photons with $\lambda <$ 3646 Å and thus reduces I[Fe II(UV)]/I[Fe II(opt)].

In our calculation we assume that the probability of local destruction is given simply by $\tau(\text{Bac})/[\tau(\text{Bac}) + \tau(\text{line})]$, where τ(Bac) and τ(line) are the Balmer continuum and Fe II line optical depths, both evaluated in a small region near the line formation zone, and only for lines with $\tau(\text{line}) > 1$. By comparing our results with those of Ferland and Netzer (1979) we find that 0.2–0.5 of the destruction occurs locally, and the rest on the way out. [This value depends on the turbulent motion through τ(line).] We also find that the relative strengths of the ultraviolet and optical Fe II lines are not very sensitive to local destruction, and, in most cases, it is quite safe to ignore local absorption. In these cases we apply the results of the Monte Carlo calculations assuming that all destruction is nonlocal. We also include this process in calculating the hydrogen level 2 population. We reemphasize that our approach is in no way a replacement for a full Monte Carlo treatment (at present unavailable) that would give the change in the level populations everywhere across the cloud. The effect is very important in calculating the Fe II emergent flux, but the local heating or cooling does not change much, at least for $N_e < 10^{10}$ cm^{-3}, since most ionization results in hydrogen recombination, reradiating most of this energy.

The relative strengths of hydrogen and Fe II lines depend on their optical depths. In a given cloud we expect a simple, almost linear, relation between $\tau(2343)$ and $\tau(\text{H}\alpha)$ (see Paper I). This relation is different for different clouds because $\tau(\text{H}\alpha)$ and τ(Bac) depend to a large extent on the ionizing flux (i.e., the distance from the ionizing source; see Netzer 1977; Ferland and Netzer 1979) and not on the ionization parameter, whereas $\tau(2343)$ depends on the Fe^+ column density. Since hydrogen is mostly neutral over the Fe^+ zone, $\tau(2343)$ is proportional to τ(Lyc). In practice the Fe II optical depth should be considered only to the point where the temperature drops below some critical value ($\sim$6000 K). This corresponds to a particular Lyman continuum optical depth and will not depend on the clouds' distances from the ionizing source. In most models that we calculated $\tau(\text{Lyc}) \leq 10^5$.

Several effects can alter $\tau(2343)$ considerably. Clouds may be truncated at large τ(Lyc) (see Mathews 1982), or the iron abundance may be different in different objects. The continuum may have an unusually high proportion of soft X-rays as compared with ultraviolet photons, as in the Kwan and Krolik (1981) and Kwan (1984) models, resulting in an extremely deep, warm ($T \sim 8000$ K) transition zone, where the temperature is high enough to excite Fe II, Mg II, and the Balmer lines, even for

[3] Full lists of all wavelength coincidences and other data used can be obtained from the authors.

$\tau(\text{Lyc}) \gg 10^5$. In this case the effective optical depths of the Fe II lines are much larger, and $\tau(\text{H}\alpha)$ depends largely on the column density. Since the extremely deep, warm transition zone is a direct consequence of the continuum chosen, and since we are not sure that such a continuum is compatible with most observations, we do not consider such models in detail.[4] Because of the dependence of $\tau(\text{H}\alpha)$ on the ionizing flux, similar (Fe^+, T_e) structure can be associated with very different Balmer opacity. This may have implications for the Fe II line profiles. That is, if cloud velocities depend on their distances from the ionizing continuum, one would expect the Balmer and Fe II(UV) line strengths to depend on velocity, since they all are sensitive to the Balmer optical depths. Optical Fe II lines are not destroyed by the Balmer continuum, and so need not depend on velocity in the same way. Therefore, their profiles may differ from those of Balmer lines.

The relative strengths of Mg II and the Fe II(UV) lines depend on the physical conditions in the extended partially ionized zone. There are two main differences between Fe^+ and Mg^+. First, the Fe^+ zone is more extended (Netzer 1980), and part of the Fe II emission comes from a higher temperature region, where most Mg is Mg^{+2}. Second, the radiative transfer of the lines is very different. The Mg II λ2798 emission is a pair of resonance lines, while Fe II emission involves thousands of transitions and rather complicated transfer and line fluorescence. An important consequence is the different amount of Balmer continuum destruction in cases where $\tau(\text{Bac}) > 0.5$. For each optically thick Fe II resonance line there are many escape routes, through conversion to other transitions with smaller optical depths. Where the Balmer opacity is small, most of these photons can easily escape. Deeper inside the cloud, Fe II excitation results in emission of optical line photons that are not subject to Balmer destruction. Mg II λ2798 is rather different. It is formed where the Balmer opacity is larger, and line photons scatter many times on the way out. Also, its wavelength is closer to the Balmer edge compared with the strongest Fe II lines. The result is that nonlocal destruction affects Mg II much more than Fe II. To illustrate this, we note that in the standard model of Paper I, with $\tau(\text{Bac}) = 0$ and $N(\text{Mg}) = N(\text{Fe})$, $I[\text{Fe II(total)}]/I(\text{Mg II } \lambda2798) = 2$. If instead $\tau(\text{Bac}) = 1$, then Fe II is reduced by a factor of 2 and Mg II by a factor of 3–4. The result is $I[\text{Fe II(total)}]/I(\text{Mg II } \lambda2798) > 3$. Our calculations show that for models with cosmic abundances and $\tau(\text{Bac}) \leq 2$, the total Fe II emission can be up to 4 times as large as that of Mg II λ2798.

Most of the above results concerning Fe II emission *cannot* be obtained in standard photoionization calculations such as those of Kwan (1984), where only a simple model for the Fe^+ atom is considered. Such models tend to produce stronger optical Fe II lines, since they do not allow for the many escape routes available for the ultraviolet photons (small optical depth transitions, fluorescence, etc.) For example, for their standard model Kwan and Krolik (1981) derive $I[\text{Fe II(total)}]/I(\text{Mg II}) = 1.3$. (Later Kwan 1984 improved the calculations and found a similar value.) We have used our photoionization code to recalculate this model, but with the full treatment of the Fe II transfer. [In this model $\tau(\text{Bac}) = 1$.] We find $I(\text{Fe II})/I(\text{Mg II}) = 3$. Most of the change is due to the increase of the ultraviolet Fe II lines, and our models also give much larger $I[\text{Fe II(UV)}]/I[\text{Fe II(opt)}]$ compared with the Kwan and Krolik (1981) model. Another very important consequence of including the more realistic Fe^+ model is the different temperature in the transition zone. Our models provide more cooling and therefore lower temperatures than are calculated in any other photoionization models. The result is weaker Lyα and Hα and other Balmer lines, and a smaller optical depth in all these transitions.

On the basis of our experience, we suggest the following simplified scheme to improve the energy-balance calculations in standard photoionization models. A three-level Fe^+ atom can be used, with ground state (level 1), a metastable level at 2.9 eV (level 2), and an odd-parity level at 4.9 eV (level 3). The statistical weights of these levels are the same. Spontaneous decay rates are $A_{21} = 1$, $A_{31} = 6 \times 10^8$, and $A_{32} = 7 \times 10^4$ s^{-1}. Optical depths should be calculated using the UV3 line at 2343 Å for 1–3 transitions, and those of multiplet 48 for 2–3 transitions, but considering only half the number of atoms, because of the large number of possible transitions. For collision strengths we take $\Omega_{12}/g_1 = 1$, $\Omega_{13}/g_1 = 12$, and $\Omega_{23}/g_1 = 6$. In most cases this scheme reproduces adequately the total Fe II emission. The relative strengths of the ultraviolet and optical lines are usually reproduced to about 30%, provided that the Balmer continuum destruction is properly considered. The collision strengths mentioned for the 1–3 and 2–3 transitions are about 3 times as large as the values usually assumed for a $\sim$10-level Fe^+ atom, and the relative A-values favor the 1–3 transition. This reflects the many escape routes available after an atom is excited to level 3.

b) Balmer Lines and Continuum

The emission of Balmer continuum in gaseous nebulae has been studied by many (e.g., Brown and Mathews 1970 and references therein). Under Case B conditions the Balmer continuum flux at the Balmer edge is proportional to $T_e^{-1.5}$, and the total emission integrated over all frequencies is given by

$$I(\text{Bac}) \approx 4.88 \times 10^{-25} T_4^{-0.5} N_e N(\text{H}^+) \text{ ergs s}^{-1} \text{ cm}^{-3} , \quad (1)$$

where $T_4 = T_e \times 10^{-4}$. Since in Case B

$$\alpha_{\text{eff}}(\text{H}\beta) \approx 3.03 \times 10^{-14} T_4^{-0.9} \text{ cm}^3 \text{ s}^{-1} ,$$

we find

$$I(\text{Bac})/I(\text{H}\beta) = 3.95 T_4^{0.4} . \quad (2)$$

Large deviations from this simple relation are expected if the optical depth in the Balmer lines is significant (Netzer 1975; Krolik and McKee 1978; Drake and Ulrich 1980; Kwan and Krolik 1981; Collin-Souffrin, Dumont, and Tully 1982; Hubbard and Puetter 1985). For example, Hβ may be weaker [low $\tau(\text{H}\beta)$, small N_e] or stronger [large $\tau(\text{H}\beta)$, large N_e] compared with a case of no Balmer optical depths. The situation is even more complex if $\tau(\text{Bac})$ is significant. In this case $I(\text{Bac})/I(\text{H}\beta)$ depends on the temperature and optical-depth structure

[4] Kwan and Krolik's (1981) continuum overestimates the observed X-ray to ultraviolet flux ratio of most objects by a large factor. (For example, Zamorani *et al.* 1981 find $\langle \alpha_{ox} \rangle = 1.3$ [the spectral index α is defined by $F_\nu \propto \nu^{-\alpha}$], which results in $F_\nu(2 \text{ keV})/F_\nu(\text{Lyc})$ about a factor of 6 smaller than the Kwan and Krolik continuum. There is an even larger discrepancy for radio-quiet QSOs, where $\alpha_{ox} \sim 1.5$.) Also, there is no clear observational evidence for an intrinsically steep ν^{-2} ultraviolet continuum as assumed by Kwan and Krolik (1981). Our observations (§ II) indicate a much flatter continuum for $\lambda > 1000$ Å in all objects, and we do not see an obvious reason to assume a large intrinisc change of slope beyond the Lyman edge. The steep Lyman continuum observed by Green *et al.* (1980) in two objects may be the result of obscuration (e.g., Eastman, MacAlpine, and Richstone 1983; Bechtold *et al.* 1984). The ν^{-2} continuum results also in a serious underestimate of the strengths of He II lines (e.g., MacAlpine 1981).

of the cloud. Recent photoionization models demonstrate the very large range expected in this ratio. For example, the Kwan and Krolik (1981) models predict $I(\mathrm{Bac})/I(\mathrm{H}\beta) = 1.6$–15. The improved calculations by Kwan (1984) cover a similar range, and recent calculations by Hubbard and Puetter (1985) and Puetter and LeVan (1982) show a very large range of $I(\mathrm{Bac})/I(\mathrm{H}\beta)$.

Several calculations of low-order Balmer line intensities are available, covering a large range in the ratios $I(\mathrm{H}\alpha)/I(\mathrm{H}\beta)/I(\mathrm{H}\gamma)$. The different results reported are largely the result of different physical conditions assumed (see Netzer and Ferland 1984). Most of these models do not list the strength of the $n > 5$ Balmer lines that are needed for comparison with the observed spectra. (Drake and Ulrich 1980 give results for all lines up to $n = 8$, but their models are for uniform density and temperature and cannot be applied to QSOs. Nebular calculations [Brocklehurst 1971] cannot be applied to QSOs because of their larger densities and Balmer optical depths.) We have therefore calculated several new QSO models that include Balmer lines up to $n = 15$. Below we discuss several aspects of these calculations.

For the range of densities ($N_e \sim$ a few $\times 10^9$ cm^{-3}) and temperatures ($0.8 < T_4 < 2$) expected in QSO clouds, all hydrogen levels with $n > 10$ are strongly coupled to the continuum by collisional ionization and three-body recombination. The populations of these levels are expected to be close to their thermal equilibrium values and the line intensities related to the Balmer continuum intensity. Consider first the case of $n > 10$ and $\tau(\mathrm{Bac}) < 1$. The level populations are given by

$$N_n = 4.15 \times 10^{-22} T_4^{-1.5} n^2 (1 + 15.8/T_4 n^2) N_e N_i b_n , \quad (3)$$

where b_n is the departure coefficient. Using equations (1) and (3) and $A_{n2} = 7.1 \times 10^9 n^{-5}$, we find

$$I(\mathrm{H}n)/I(\mathrm{Bac}) \approx 132 T_4^{-1} n^{-3} (1 + 15.8/T_4 n^2) \times (0.25 - 1/n^2) b_n f(\tau_n) . \quad (4)$$

In equation (4) $f(\tau_n)$ is a function of the optical depth in the nth Balmer line [for very small optical depths $f(\tau_n) = 1$]. For a thermal profile

$$\tau(\mathrm{H}n)/\tau(\mathrm{H}\beta) \approx 4.7 \times 10^{-10} (\lambda_n/n)^3 , \quad (5)$$

where λ_n is in angstroms. Many QSO models require $\tau(\mathrm{H}\beta)$ of the order of 10^3, so Balmer lines up to $n \sim 30$ will have significant optical depths. This helps to bring the level populations close to their LTE values, but, since collisional transitions are still the fastest, we expect $f(\tau_n) < 1$. An additional complication is the very large departure coefficient of level 1, and the coupling of higher levels to the ground and $n = 2$ states by optically thick transitions (e.g., Hubbard and Puetter 1985). It is therefore expected that $b_n > 1$ in parts of the cloud and for many levels. The function $f(\tau_n)$ includes this effect too.

We have carried out detailed calculations of the strengths of Balmer lines and continuum under a variety of conditions. The method used has already been described by Netzer (1980) and in Paper I (see also Netzer and Ferland 1984). In addition to the standard multi-ion temperature and ionization solution, we now solve for a hydrogen atom with 15 levels and continuum, taking into account transfer in all lines by using a local escape probability approach. This is similar to the method used by Kwan and Krolik (1981) except for the addition of many more levels and the inclusion of three-body recombination.

The Balmer continuum emission is calculated with its exact frequency dependence in every zone, as defined by the local temperature. The photons are emitted isotropically, and the emergent flux is calculated taking into account the optical depth at the frequency and direction of the emitted photons. The transfer of the diffuse Balmer radiation is calculated by a modified "outward only" method. All the outgoing Balmer flux, together with that fraction of the inward-going flux that is absorbed on the way out, is added to the outgoing nonthermal radiation field and is allowed to interact with the gas.

Figure 1 shows some of our results for the particular case of a two-component continuum: An ultraviolet component of $F_\nu \propto \nu^{-0.5}$ with an exponential cutoff at 20 rydbergs, and an X-ray component, $F_\nu \propto \nu^{-0.7}$. (This model has a very flat ultraviolet component compared with others recently studied. The justification for this is given elsewhere [Netzer 1985]). The relative flux of the two components is adjusted at 1 rydberg to give $\alpha_{ox} = 1.2$ (i.e., a single power law connecting 2500 Å with 2 keV has a slope of α_{ox}). We explore different conditions by changing the model in three ways: (1) varying the cloud thickness (i.e., τ_{912}), (2) varying the ionization parameter while keeping the density and cloud thickness constant, and (3) varying the gas density while keeping the ionization parameter and τ_{912} constant. All of our models have constant gas pressure, and the standard case has $\tau_{912} = 10^5$, $N_\mathrm{H} = 10^{9.5}$ cm^{-3}, and ionization parameter $U_1 (\equiv F_{912}/hN_\mathrm{H}) = 1.2 \times 10^8$ cm s^{-1}.

We have calculated other models with different ionizing continua and found that they vary in a similar way. The strengths of the high-order Balmer lines, as well as that of the Balmer continuum, is the largest in extreme cases, i.e., very low ($N_\mathrm{H} < 10^{8.5}$ cm^{-3}) or very high ($N_\mathrm{H} > 10^{10}$ cm^{-3}) densities, very small or very large total column densities, and very small or very large ionization parameters. This is easy to explain because Hβ is weakest when $\tau(\mathrm{H}\beta)$ is very small, or very large, and when the density is high enough to collisionally de-excite level 4. The high-order lines follow the Balmer continuum intensity very closely in these models, and in more extreme cases not shown here.

We have used the calculations to define $f(\tau_n)$ for all lines with $n \geq 15$. Each line is assigned an effective optical depth, $\tau_n(\mathrm{eff})$, and we assume that

$$f(\tau_n) = \{1 - \exp[-\tau_n(\mathrm{eff})]\}/\tau_n(\mathrm{eff}) , \quad (6)$$

where $\tau_n(\mathrm{eff})$ represents an average over different opacity zones, some (in the H$^+$ zone) with very small optical depths. It is therefore considerably smaller than the total optical depth in the line. We determine its best value by comparing equation (4) with the actual calculations for H14.[5] The merging of high-order lines with the continuum has been explicitly calculated only for nebular cases (Seaton 1964). For QSOs it has been adumbrated (Grandi 1981; Kwan and Krolik 1981; Gaskell 1981; Puetter *et al.* 1982, Malkan and Sargent 1982) that broadened Balmer lines near the series limit from an apparent continuum shifting the true limit to longer wavelengths. Here we prove this conjecture.[6] Considering Stark broadening only,

[5] An equivalent way to describe the line intensity is to define, for each, an excitation temperature (e.g., Kwan and Krolik 1981). In the case of the high-order Balmer lines $T_\mathrm{ex} \approx T_e$, and the difficulty in calculating the emergent flux is the result of different line profiles in zones of different optical depth. The $f(\tau_n)$ can be thought of as line-profile correction functions.

[6] See Krolik and McKee (1978) for the effects of the low-frequency nonthermal continuum.

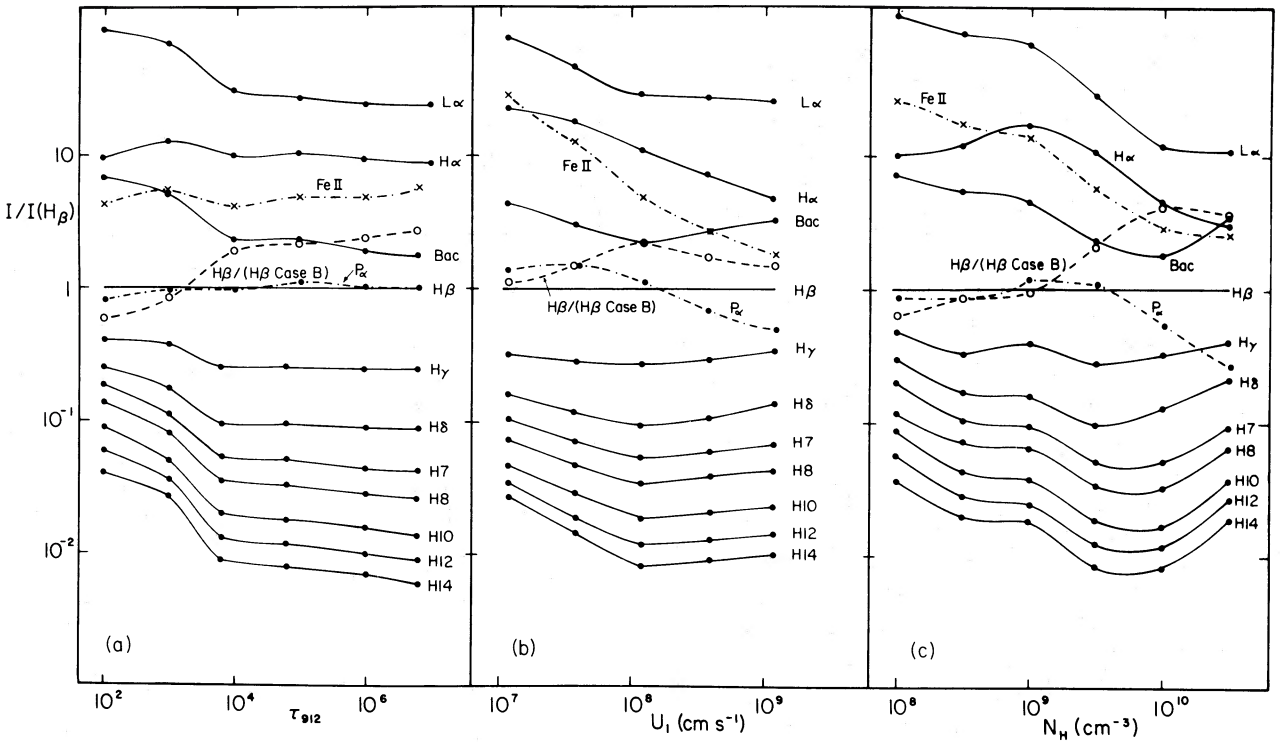

FIG. 1.—Intensities of hydrogen lines, total Balmer continuum, and all Fe II lines relative to Hβ in a standard, constant-gas-pressure photoionization model with a two-component ionizing continuum as described in the text.

the Balmer line of maximum quantum number to be resolved, n_{max}, is given by

$$\log n_{max} = 3.128 - 0.133 \log N , \quad (7)$$

where $N = 2N_e$ for $T < 10^5/n_{max}$ and $N = N_e$ for $T > 10^5/n_{max}$ (Lochte-Holtgreven 1958). For QSO densities, $n_{max} \approx 70$ and lines with larger n should not be considered. (Broad QSO lines may force even smaller n. For 1000 km s^{-1}, $n = 40$ is quite adequate.) We take all levels up to n_{max} to ensure a smooth transition near 3646 Å. The exact number of lines is not important, since their n^{-3} dependence ensures rapid convergence and small increase in total intensity near the limit. Our calculations (see § IV) show a smooth transition of high-order lines to the continuum. The rise over the nonthermal continuum starts longward of about 4000 A (depending strongly on the importance of the broad line wings), in good agreement with the observations.

The Balmer continuum flux distribution is an important consideration. The optically thin distribution is a well-known function of temperature, but the observed flux is from regions of different temperature and τ(Bac). Some model calculations are available (Puetter and LeVan 1982), but only for a simple uniform density and uniform temperature case. Our model calculations give the shape of the emergent Balmer continuum. We assume a symmetrical distribution of clouds around the continuum source with no shadowing of one cloud by another. Although the transfer method used is not very accurate, it is probably good enough for τ(Bac) ≤ 2. The main advantage of such calculations over existing models is the averaging over many zones of different temperatures. For the purpose of model fitting we use a single-temperature empirical formula (as used also by Grandi 1982) given by

$$F_\nu(\text{Balmer}) \propto B_\nu(T_e)(1 - e^{-\tau_\nu}) . \quad (8)$$

Comparison with our calculated continuum shows equation (8) to be quite satisfactory when we use an average model temperature and take τ(Bac) to be *twice* the calculated value. For the model in Figure 1, τ(Bac) = 0.5, and most of the Balmer continuum arises in the H^+ zone. The effective temperature in this case is ~15,000 K. Even higher temperatures are typical of small density and/or small τ_{912} cases. Models with larger X-ray flux and larger Balmer optical depths produce most of the Balmer continuum in regions where $T \sim 10^4$ K. However, because of the larger optical depths, the shape of the Balmer continuum is also similar to that of the high-temperature cases. This was also realized by Puetter *et al.* (1982) in their analysis of 3C 273. (Note here that two-photon emission is negligible in all our calculations.)

Another process that was not considered previously is the absorption of Balmer continuum photons by Fe^+. At least half of the Balmer continuum passes through a region where τ(2343) is very large, and so will be partly absorbed by Fe^+. The total energy absorbed is quite small for $V_t < 20$ km s^{-1}, but the effect on the observed strengths of individual features can be rather large, as seen in Figure 2. Since the strongest Fe II emission lines are also those with the largest optical depth, the emergent spectrum near their wavelengths is significantly affected. We include this process in our model calculations and spectrum fitting, as shown in § IV. We note that this effect can be significant in objects such as symbiotic stars or novae where both the Fe II(UV) lines and the Balmer continuum are strong at some phases.

III. OBSERVATIONS

We have obtained good-quality spectra (signal-to-noise ratio up to 200:1) of bright QSOs (<16.5 mag), in order to investigate the most important Fe II features and other broad lines that lie between rest wavelengths of about 2000 and 5000

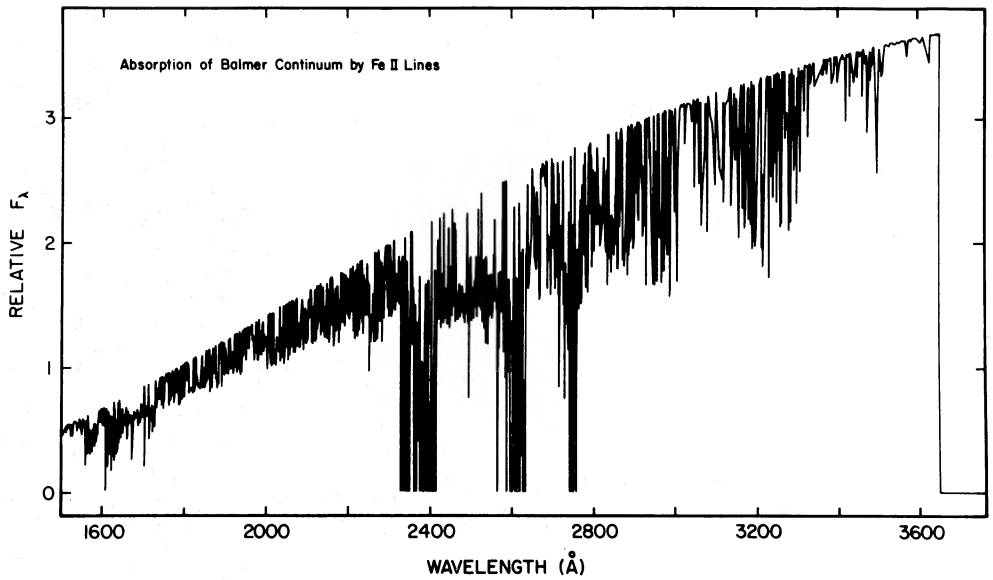

FIG. 2.—The absorption of a 15,000 K, optically thin Balmer continuum by Fe^+. All the Balmer continuum is assumed to pass through a typical QSO Fe^+ zone. The bin size is 1 Å, so Fe II lines with equivalent widths ≥ 1 Å absorb all the continuum at that wavelength.

Å. Most have redshifts $0.46 < z < 0.7$, although two lower-z objects with *IUE* observations are included. The spectra always included Hβ, and sometimes C III] λ1909. Except for the *IUE* data, the wavelength resolution is $\sim$8 Å (FWHM, observed frame), and the accuracy of the relative flux calibration is 5–10% over most of the spectrum, but may be more than 10% near the atmospheric cutoff at 3200 Å, or $>$7500 Å, where a smaller spectrograph aperture was used to reduce the effects of variable atmospheric water-vapor emission, and where standard star fluxes are less certain. The characteristics of the spectrograph and image dissector scanner (IDS) detector, used on the 2.7 m reflector of the University of Texas McDonald Observatory, and the techniques of observation and data reduction, are described in the Appendix.

Some of these spectra have been extended to ultraviolet and infrared frequencies as part of a related program to investigate QSO continua. These additional data include (almost) line-free regions of the spectrum and have therefore been used to constrain the continuum level beneath the Fe II and Balmer lines and the Balmer continuum. In this paper we present only a few typical examples of QSO Fe II spectra; others will be discussed in a later paper.

The spectra are shown in Figure 3 and are discussed in § IV. Galactic extinction corrections have been applied, and two examples are given of spectra with and without corrections for possible additional (intrinsic) extinction.

IV. FITTING OF THE MODELS TO THE OBSERVED SPECTRA

We now describe the procedures used to fit Fe II and Balmer continuum models to the observed spectra. The purpose is to show that the models can provide a good fit to the spectra of many QSOs, within observational and model uncertainties, and to obtain the strengths of all emission features. However, the large number of Fe II lines makes it impossible to treat them individually. We found that spectrum fitting, i.e., a match of Fe II models to the data, is the only reliable way to measure the strengths of these lines. In other words, prior knowledge of the Fe II spectrum is essential. In this way, the power-law continuum, the Fe II model, and the Balmer continuum with higher order lines are fitted independently. Other lines (e.g., C III] λ1909, Hβ, Hγ, ...) are included with intensities that best fit the observed spectrum, with no relation to the theoretical results. Their strengths relative to the Fe II and Balmer emission are then compared (§ V) with model predictions. We emphasize that *a range of models can fit a given observed spectrum.* There are several free parameters, so it is not possible to determine precise values of, e.g., τ(2343) and τ(Bac), but there are some general properties of the Fe II and Balmer emission that emerge from this comparison of the models with the data.

Since we are concerned with the ability to fit the observations over the relatively small rest-wavelength range of about 2000–5000 Å, we have, justifiably, approximated the continuum underlying the blended emission lines by a power law, although curvature of the continuum due to the contribution of the infrared excess becomes important for $\lambda > 5000$ Å (the exact wavelength depending on the particular spectrum). The inappropriateness of this power-law approximation over larger wavelength ranges will be discussed in another paper (Wills *et al.*, 1984; see also Neugebauer *et al.* 1979; Malkan 1983; Oke, Shields, and Korycansky 1984). The exact means of estimating the continuum levels depends on the range of rest wavelengths available. Continuum levels can be chosen immediately beyond Hα, between 5400 and 6200 Å, from 1430 to 1460 Å, and from 1330 to 1380 Å, since they seem relatively free of Fe II and other emission lines. For four of the spectra *IUE* data are used to constrain the ultraviolet continuum, although the relative *IUE* optical calibration uncertainties and noisy *IUE* data introduce uncertainty. For other spectra the ultraviolet continuum was not as well defined and was estimated in the region of C III] λ1909, where the Fe II(UV) lines contribute much less with decreasing wavelength for a wide range of models (Paper I). The continua of all spectra presented here are quite well constrained near or beyond 4500 Å. Strengths of optical features between 4000 and 4600 Å scale similarly with τ(2343) and τ(Bac) (see Paper I). This means that the strength of the 4570 Å feature can be used to estimate the strengths of Fe II features underlying Hγ and Hδ. Thus we can estimate the continuum level in this wavelength region. Where more than two contin-

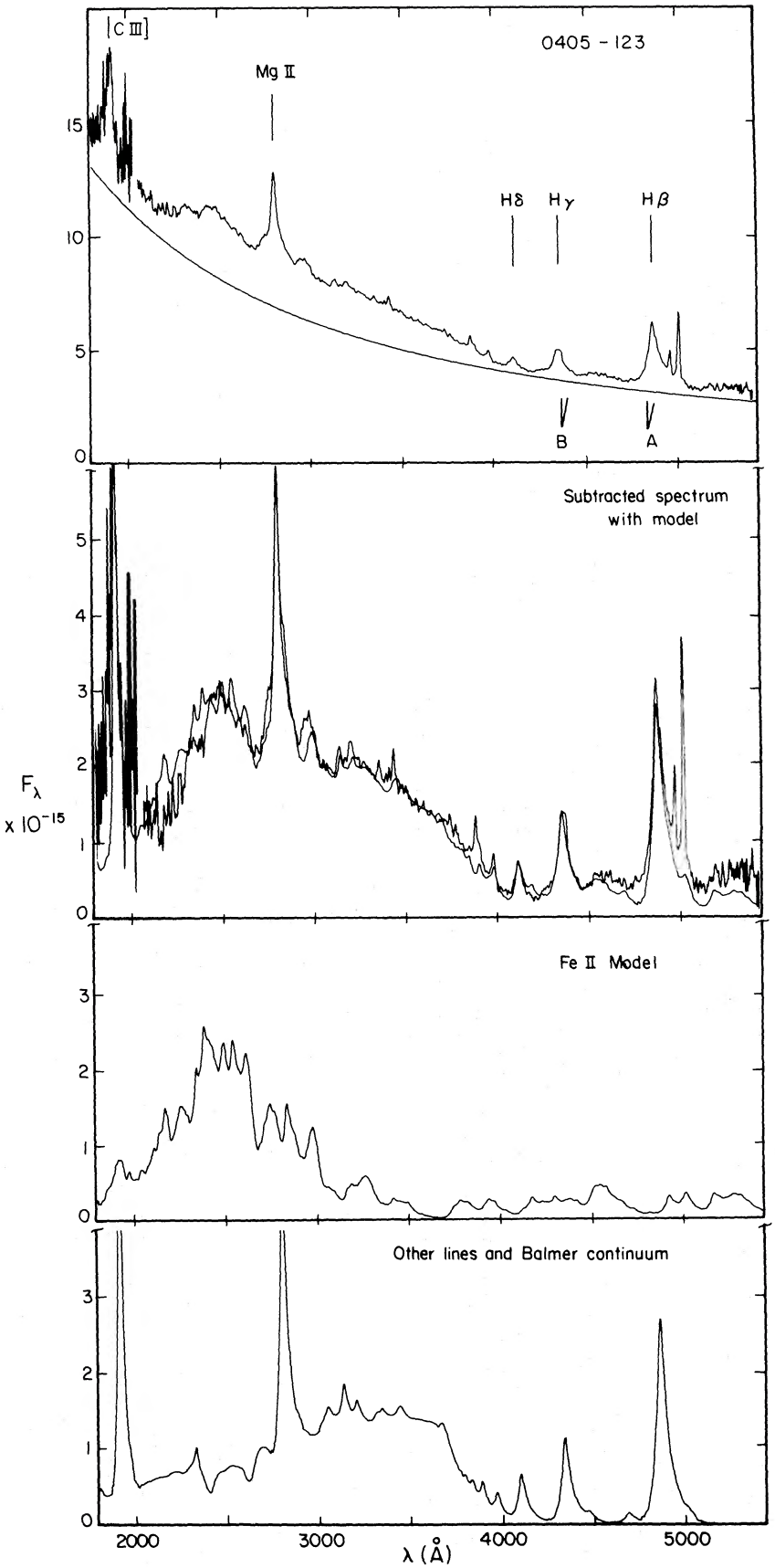

FIG. 3a.—Spectra of 0405 – 123. The region of C III] is from *IUE* data.

FIG. 3.—Nine spectra models for QSOs. For each QSO spectrum, the upper panel gives the observed flux (ergs s^{-1} cm^{-2} $Å^{-1}$) as a function of rest wavelength, after correction for galactic extinction. The power law used in the modeling is shown. The second panel shows the same spectrum with the power law subtracted and a synthetic broad-line spectrum superposed. The hydrogen Balmer lines and the C III] λ1909 and Mg II λ2798 lines are indicated, as well as the regions of the spectrum that have been corrected for the atmospheric A and B bands. Narrow lines of [Ne V] λλ3346, 3426, [O II] λ3727, [Ne III] λλ3869, 3968, [S II] λλ4069, 4076, and [O III] λλ4363, 4959, and 5007 and narrow Balmer lines are often present but are not included in the models. The third and fourth panels show the components of the synthetic broad-line spectra for Fe II, and for all other broad lines combined with the Balmer continuum.

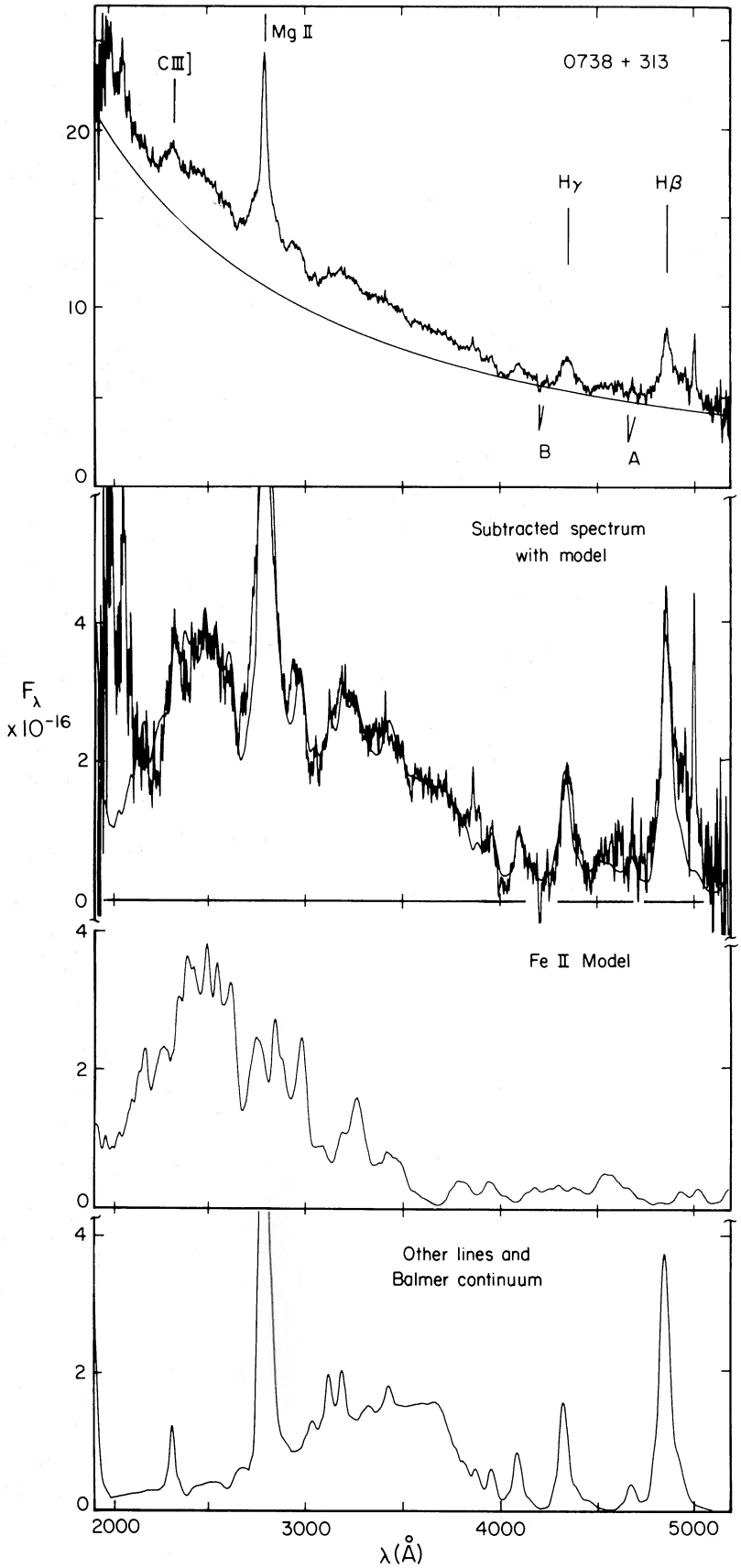

FIG. 3*b*.—Spectra of 0738 + 313

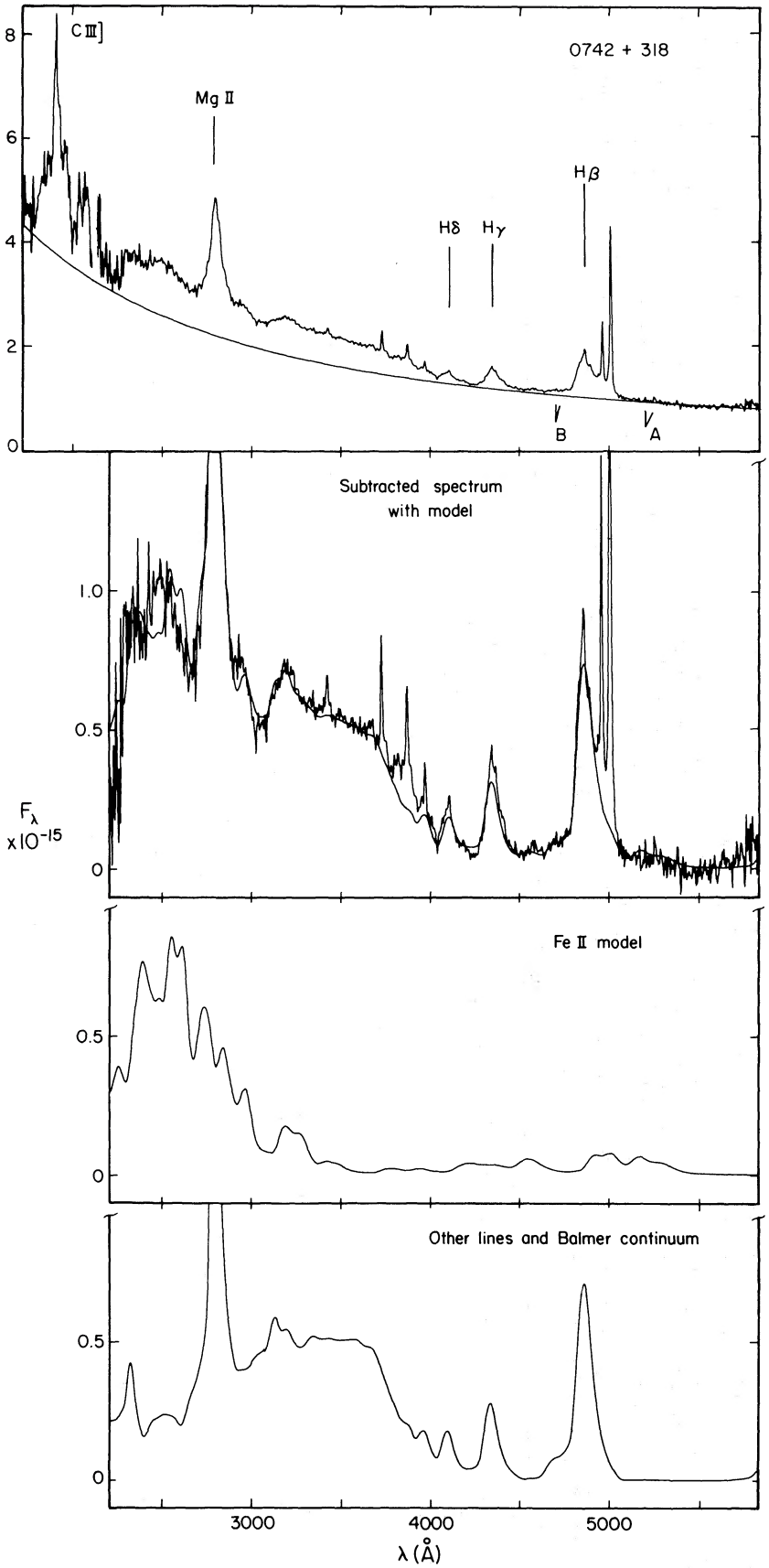

FIG. 3*c*.—Spectra of 0742+318 with no intrinsic extinction

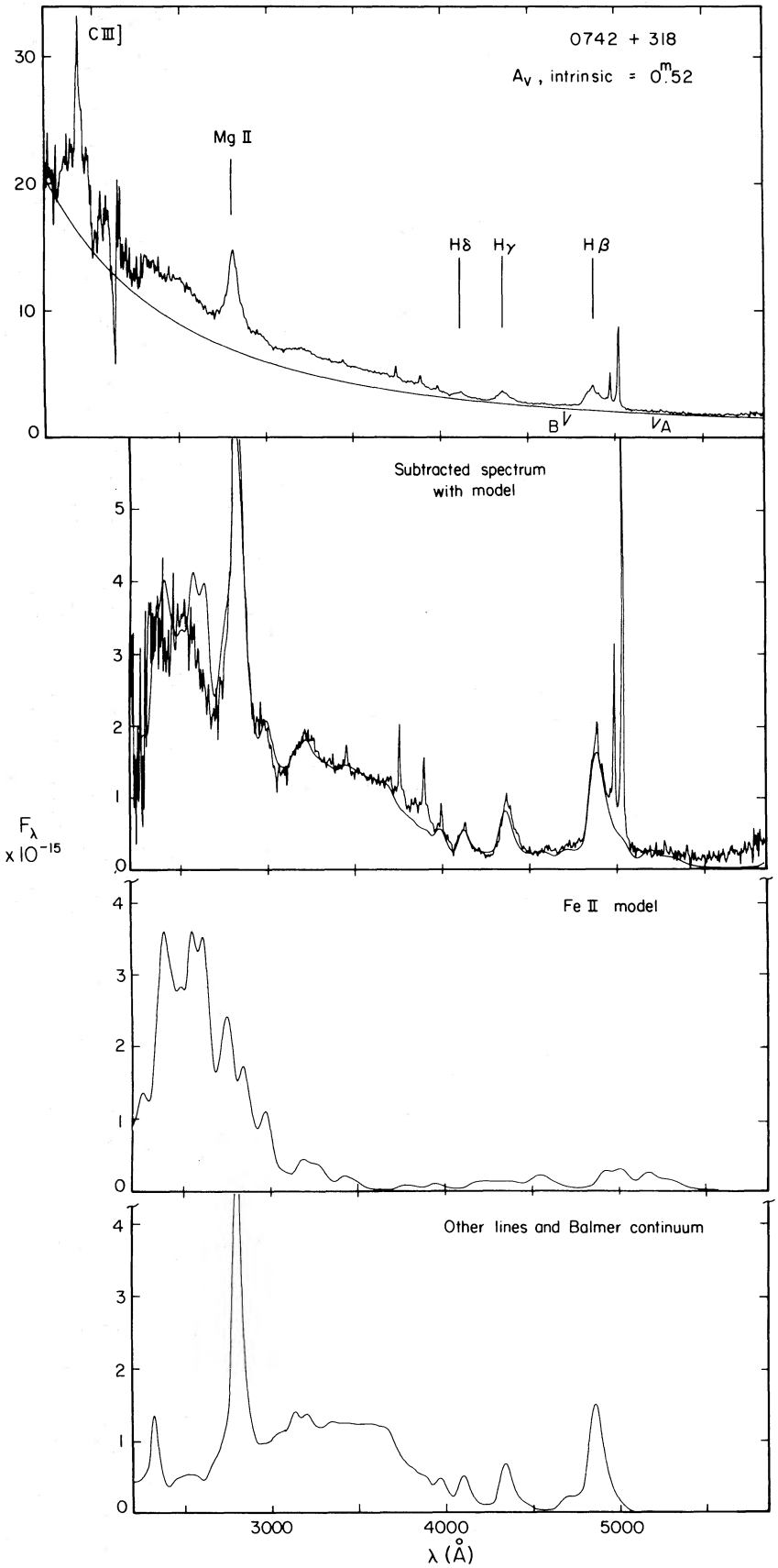

FIG. 3*d*.—Spectra of 0742+318 with entire spectrum corrected for $A_V = 0.52$ mag according to a λ^{-1} extinction law. The region near C III] is from *IUE* data.

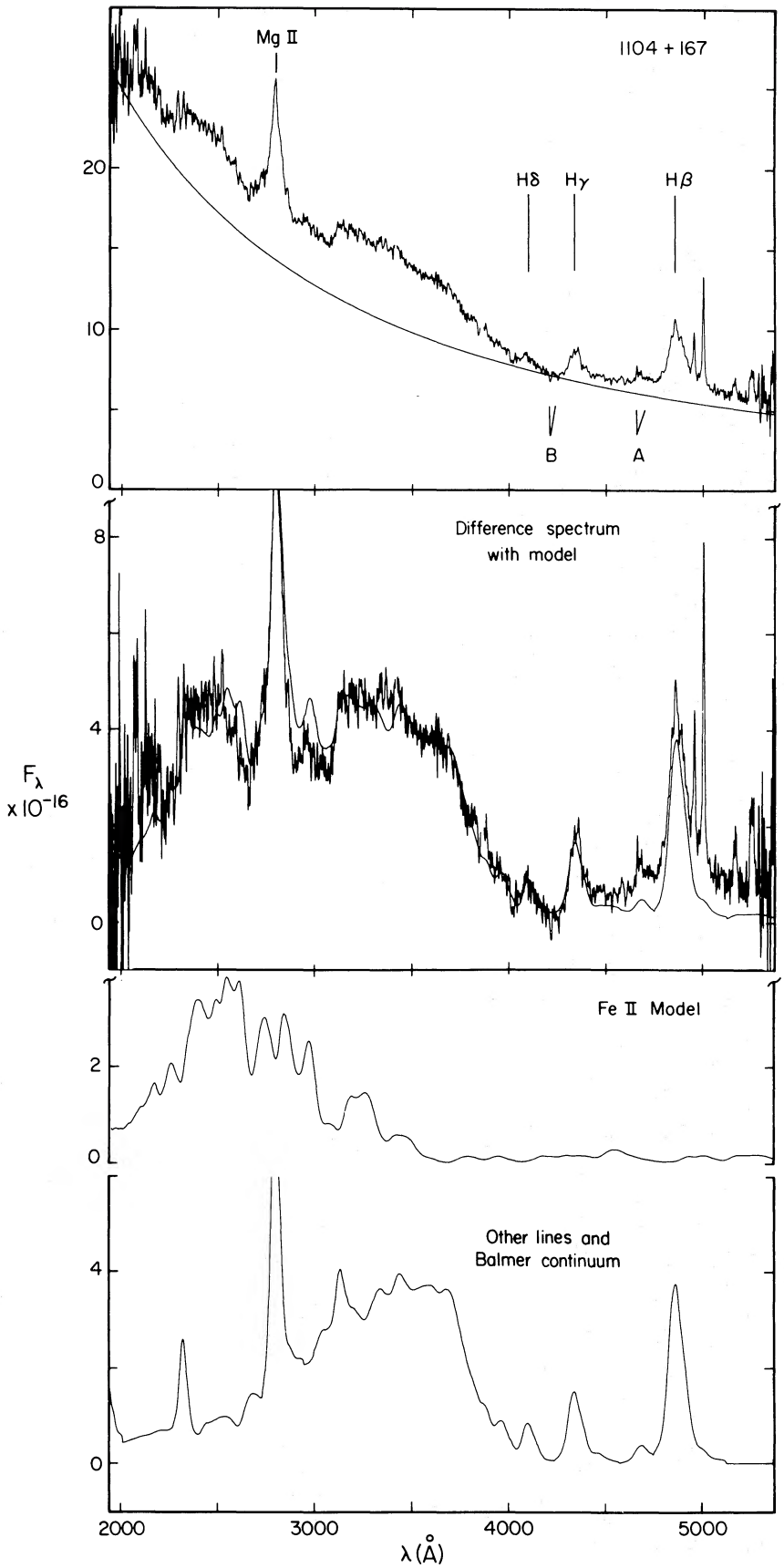

FIG. 3*e*.—Spectra of 1104+167

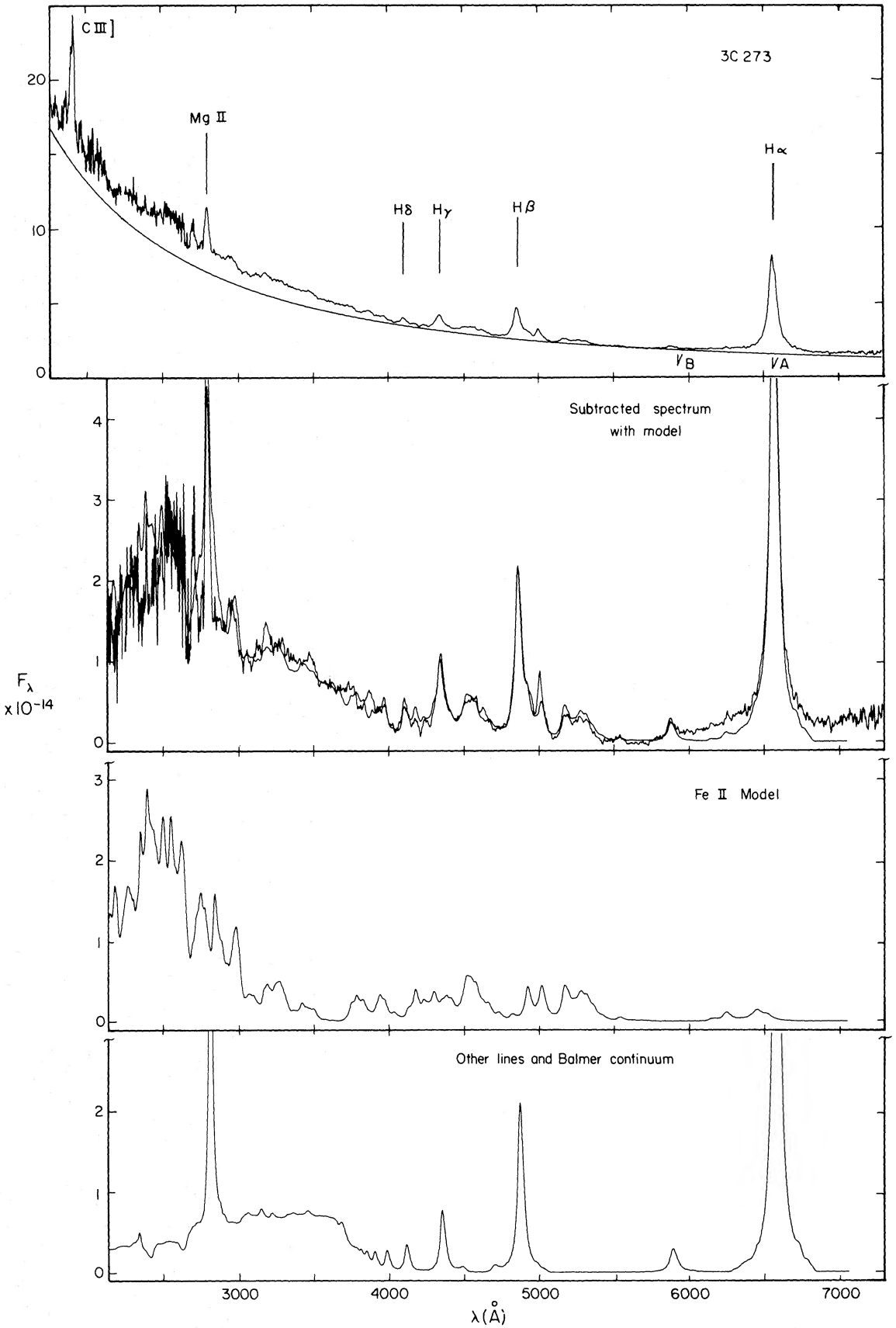

FIG. 3f.—Spectra of 3C 273 without intrinsic λ^{-1} extinction

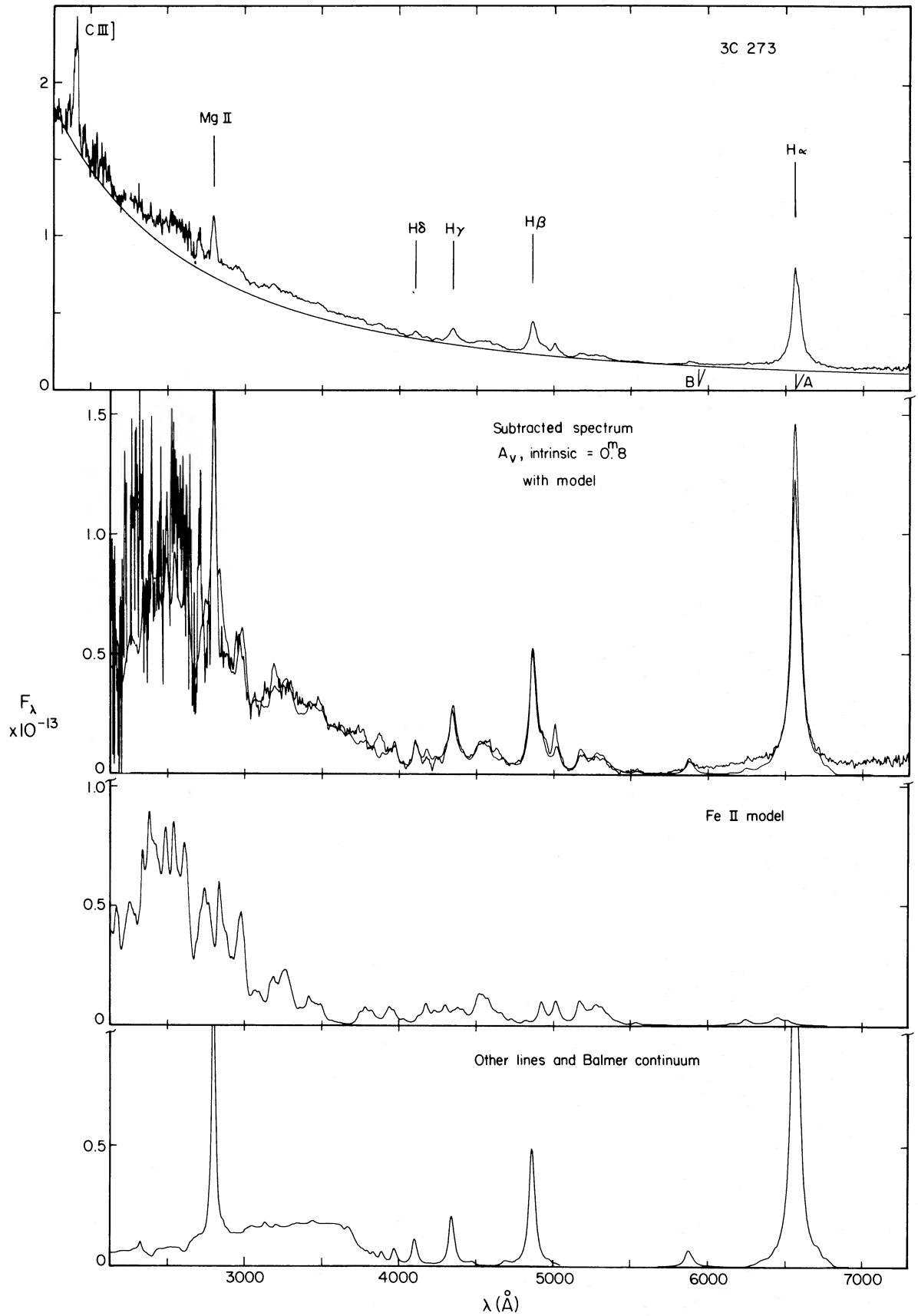

FIG. 3*g*.—Spectra of 3C 273 with intrinsic λ^{-1} extinction; $A_V = 0.8$ mag for the power-law–subtracted only. The *IUE* data are the best calibrated spectra from Ulrich *et al.* (1980).

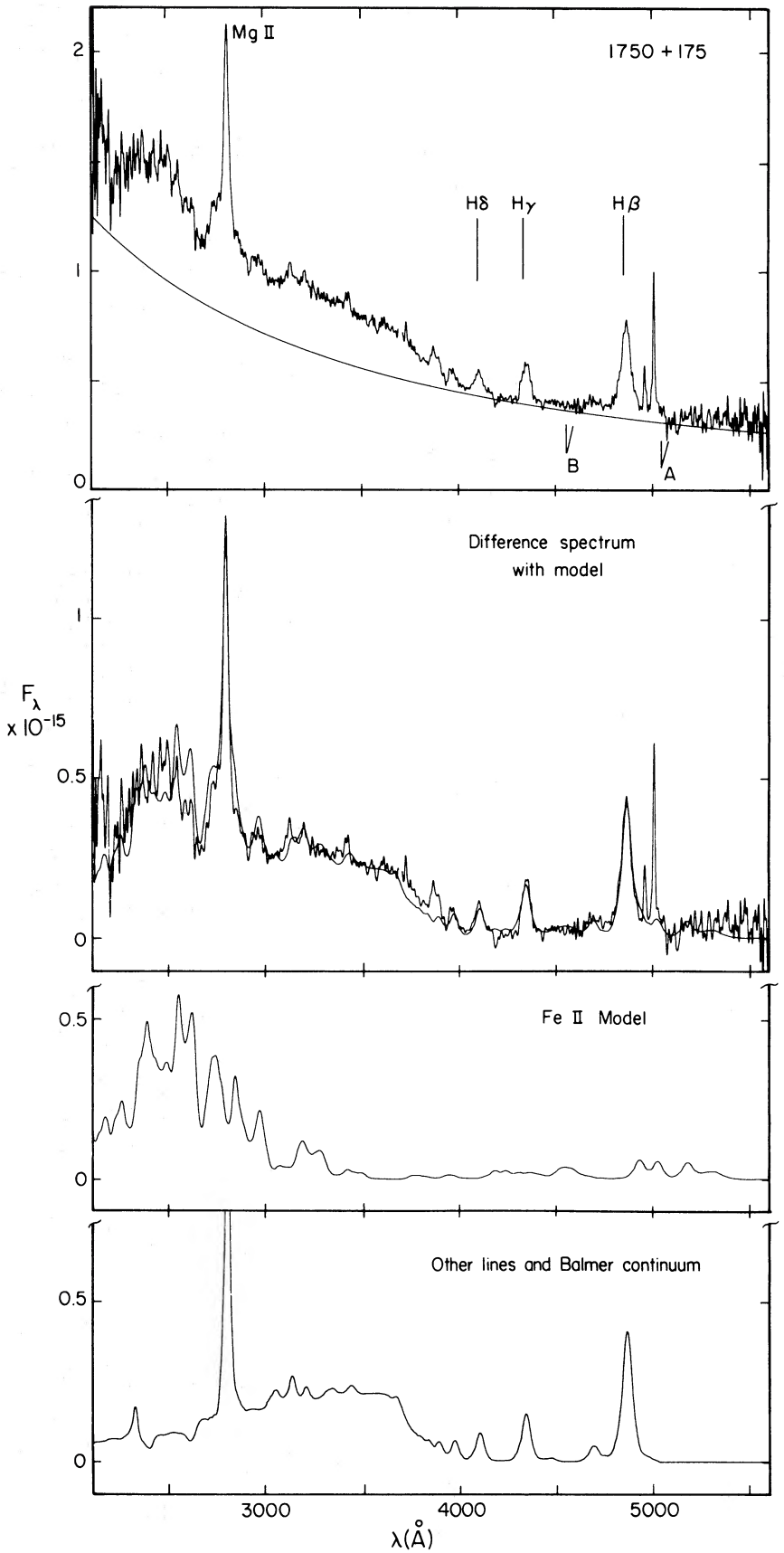

FIG. 3*h*.—Spectra of UT 1750+175

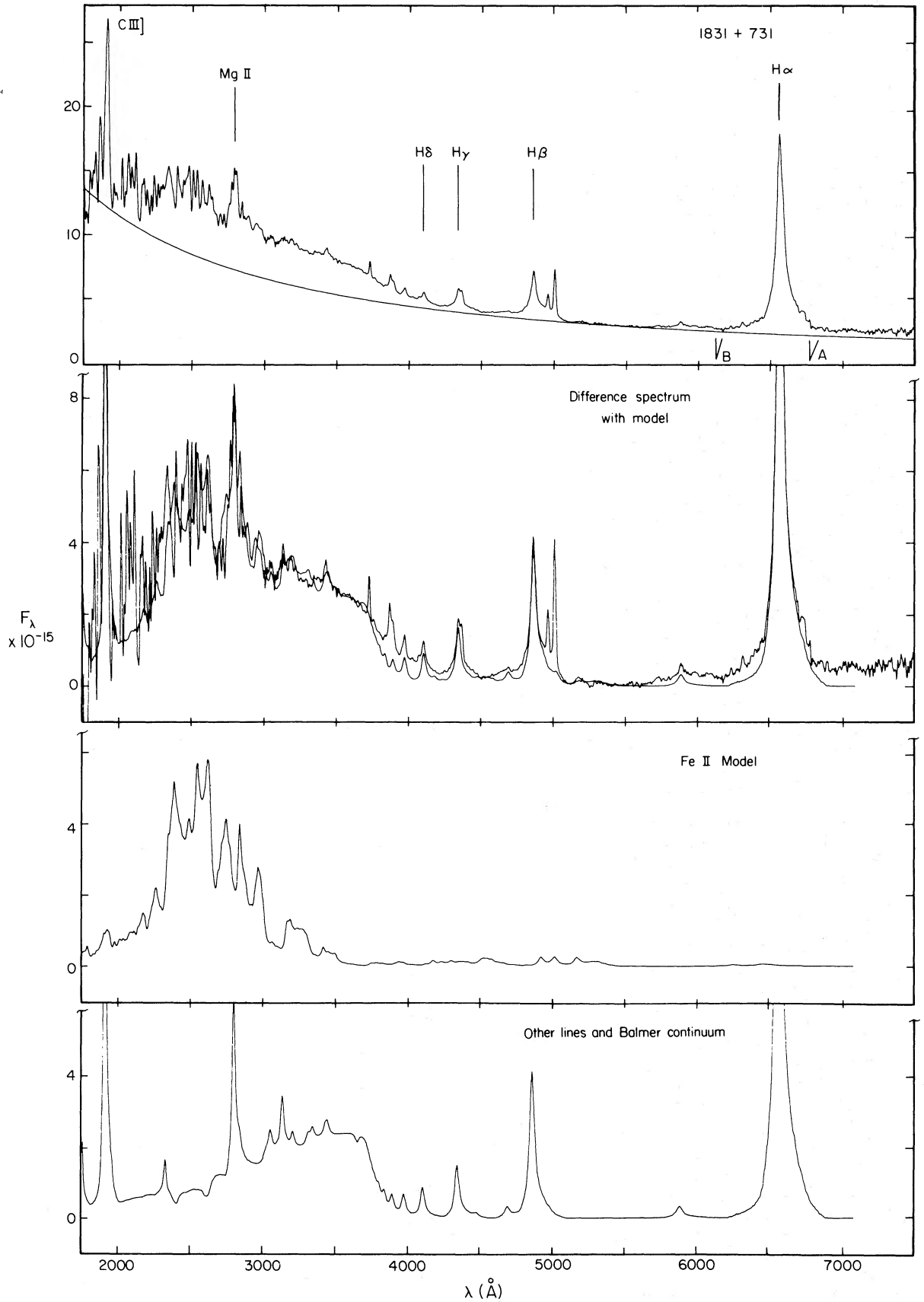

FIG. 3*i*.—Spectra of 1831 + 731. The *IUE* and optical spectra overlap at Mg II.

uum points could be determined, the fit was consistent with a power law over the wavelength range of interest.

We note that, luckily, there is almost no contribution from Fe II near 3675 Å[7] (see Fig. 3), and that this is very closely the wavelength corresponding to the maximum contribution of the Balmer continuum, taking into account the broad QSO line profiles and the merging of the high-order Balmer lines. Thus the observed excess flux at this wavelength, above the power-law continuum, combined with Balmer continuum temperatures and optical depths from the models, defines the Balmer continuum. We are thus able to estimate the total strength of the Balmer continuum quite well, with important implications for the broad-line region (BLR) covering factor (see § V).

We next *measure* from the observed QSO spectrum the strengths of strong lines—Mg II λ2798, Hδ, Hγ, Hβ, He II λ4686 (usually an upper limit), and sometimes Hα and C III] λ1909. We estimate the strengths of other weaker lines (e.g., C II] λ2326, O III resonance fluorescence lines between 2820 and 3444 Å, He II λ3203, and He I λ4471) from photoionization models. These, together with the Balmer continuum and power-law continuum defined as described above, allow a first estimate of the strengths of the Fe II(UV), Fe II(3000–3500) and Fe II(opt) lines, and thus a specific Fe II model.

Once we have a list of line strengths for Fe II and other lines and the Balmer and power-law continua, we proceed to convolve these with a realistic line velocity profile. The least blended strong line was Hα, available for 3C 273 and 1831+731, and this line was used directly to determine a velocity profile. (We could see no evidence for [N II] $\lambda\lambda$6548, 6584, so we have assumed its contribution to be unimportant.) In all other spectra Hβ was the least blended line, but because Fe II multiplets may contribute to the long-wavelength side of Hβ, and [O III] $\lambda\lambda$4959, 5007 are present in the red wing, it is necessary to remove their effects iteratively. We note that, for a wide range of models, a pair of relatively isolated Fe II features near 5200 Å are similar in strength to the pair at 4990 Å [although the longer wavelength member of the 5200 Å pair decreases in strength for smaller τ(2343)]. Given the observed strengths of the Fe II $\lambda\lambda$4570 and 5200 features, we can model the Fe II emission and subtract the Fe II λ4990 from the Hβ and [O III] profiles. The [O III] lines are generally thought to arise in the low-density ($n_e = 10^4$–10^6 cm^{-3}) narrow-line region. Thus our first attempts to remove their contribution to the blend (with Fe II subtracted) assumed that the Hβ red wing was defined quite well by fluxes at wavelengths $<$4940 Å, near 4971 Å, and $>$5020 Å. In some cases this derived Hβ profile had a very large red wing, quite inconsistent with profiles of Mg II λ2798 plus Fe II, or Hγ plus [O III] λ4363 plus Fe II blends. In those cases we artificially forced the positive velocity profile to decline more rapidly and smoothly. A broad-line contribution from the [O III] would provide a ready explanation for this anomaly. This velocity profile was convolved with the Fe II model, with the Balmer continuum, and with other lines, to produce a synthetic spectrum, which was then compared with the observed spectrum, after subtraction of the power-law continuum. Usually only small modifications to the Fe II model or Balmer continuum were required to perfect the match.

The results of the fitting are shown in Figures 3*a*–3*i*. The spectra, corrected for Galactic extinction, are shown with the adopted power-law continua, then with this underlying continuum subtracted and a possible synthetic spectrum superposed. Shown separately beneath are the Fe II synthetic spectra and the synthetic spectrum of the combined Balmer continuum (with absorption by high-optical-depth Fe II) and other broad lines. Two cases with the observations corrected for intrinsic extinction are also shown (see below). Table 1 gives absolute and relative strengths for all measured spectral features. The strengths of Fe II blends, the Balmer continuum, and high-order Balmer lines (H8–H14, H15–H$n_{\rm lim}$), are taken from the fitted models shown in Figure 3. Profile fitting has been used to measure the strengths of relatively isolated lines and lines in *IUE* spectra, after subtracting the Fe II emission. The strengths of very blended lines have been determined from the model fitting. Thus the Mg II λ2798 and Balmer line strengths (H3–H7) should be more reliable than previously published values.

The exact line intensities are, of course, sensitive to the choice of continuum, which is dependent on the Fe II model, and are also sensitive to the adopted line profile, especially the contribution of the broad wings. This is most serious where the high-order Balmer line wings blend with each other ($n \geq 5$). Another source of uncertainty is the contribution of the narrow lines. Where possible, the line measurements of Table 1 refer to the broad lines; however, accurate separation is often not possible. An exception is, e.g., for Hβ in 0742+318. The uncertainties in line measurements, *for a given* Fe II *model and line profile*, are indicated by letters placed alongside the measured values: a = ~5%, b = ~10%, c = ~20%, and d = ~30%. These do not include the flux calibration uncertainties. Values followed by a colon are very uncertain, and the very existence of lines given a double colon is in doubt.

We have assumed that the adopted line profile is representative of all broad lines. This may not be the case for He II λ4686, where a broader feature would better fit the data, e.g., in 1831+731, 0405−123, and 1750+175; a number of blended narrow lines could contribute to this feature in a few cases where the narrow-line spectrum is very strong (e.g., Osterbrock and Cohen 1982). Excess emission above the model, often seen near 3860 Å, is readily attributed to Fe I. A weaker Fe I feature is expected near 3710 Å, sometimes introducing uncertainty in measuring the high-order Balmer lines.

Also given in Table 1 are the parameters of the models shown in Figure 3. For the Fe II model we give v_t and $\tau_{\rm des}$, the optical depth (at the Balmer edge) used to calculate the destruction of Fe II(UV) photons by ionization of hydrogen from the $n = 2$ level. We do not attach much significance to the precise values of the parameters because different photoionization models can lead to similar Fe II spectra. For the Balmer continuum we give the effective optical depth at the Balmer edge and the effective Balmer continuum temperature. These optical depths are not the same, probably because the Fe II and Balmer continuum models are fitted independently and because for the Balmer continuum it is difficult to distinguish between low τ–high T and high τ–low T cases over the wavelength range of the fits. These optical depths could really be different if there were an asymmetric distribution of clouds around the central continuum source. (Our models assume symmetry.)

We have investigated the effects of small amounts of intrinsic extinction for the spectra of 3C 273 and 0742+318, using a λ^{-1} extinction law. For 0742+318 we have corrected the whole observed spectrum, using $A_V = 0.52$ mag in the QSO rest frame, and for 3C 273 we used $A_V = 0.80$ mag to correct just

[7] There is possibly a small contribution from Fe I near this wavelength.

TABLE 1

BROAD-LINE MEASUREMENTS AND MODEL PARAMETERS[a,b]

	0405−123	0738+313	0742+318	0742+318	1104+167	1226+023	1226+023	1750+175	1831+731
A_V(Galactic)	0.08	0.17	0.16	0.16	0	0.16	0.16	0.30	0.32
A_V(intrinsic)	0	0	0	0.52	0	0	0.80	0	0
Lα	8.0 b	...	11.5 c	25 c	...	10.8 b	97. b	...	9.0 c
C III] λ1909	1.1 c	...	1.9 d	3.1 d	...	1.45 c	5.5 c	...	1.5:
C II] λ2326	<0.1	0.12:	0.15:	0.3::	0.24::	...	...	0.12::	...
Mg II λ2798	0.81c	1.35c	1.45c	1.60c	0.95c	1.35c	1.4 c	1.30c	0.72:
Bac	9.5	4.65	7.78	8.34	8.7	7.6	6.31	9.1	9.5
H 15 − n_{lim}	0.38	0.35	0.37	0.41	0.60	0.26	0.31	0.44	0.56
H 8−14	0.48	0.49	0.57	0.61	0.85	0.36	0.33	0.50	0.61
H 7	0.10:	0.12:	0.16:	0.20d	0.16:	0.01:	0.08:	0.13:	0.13::
H δ	0.20c	0.19:	0.20c	0.27c	0.18c	0.14c	0.19c	0.19c	0.20:
H γ	0.38b	0.38c	0.35b	0.40b	0.36b	0.33b	0.38b	0.33b	0.33b
He II λ4686	<0.05	<0.15	<0.07:	<0.1:	0.10:[d]	<0.05	<0.05	0.12:	0.07:
H β	1 a	1 b	1 b	1 b	1 b	1 a	1 a	1 b	1 a
H α	3.7[c]	...	5.1[c]	4.4	...	3.8 b	2.94b	...	5.1 a
Fe II (UV)	6.53	7.3	5.05	9.75	5.7	9.8	13.7	8.6	8.5
Fe II (3000-3500)	0.85	1.45	0.51	0.74	1.2	1.1	2.0	0.83	1.3
Fe II (opt)	1.66	1.53	0.65	1.21	0.6	2.89	2.91	<1.1	<0.7
Fe II (total)	10.1	11.4	6.92	13.1	8.1	13.7	18.7	11.8	11.5
Fe I (λλ3710, 3860)	0.1	0.1	0.1	0.1	0	0.2	0.24:	...	...
W(H β)[e]	116	117	128	143	118	72	171	140	94
I(H β)[e]	27.8	5.20	13.1	6.71	27.7	175	412	4.58	32.5
z	0.5727	0.631	0.461	0.461	0.630	0.158	0.158	0.507	0.1225
F_ν(Ba edge)/F_ν(power law)	0.29	0.23	0.32	0.41	0.32	0.17	0.41	0.42	0.46
α	+0.53	+0.31	+0.61	−0.28	+0.33	+0.10	−0.02	+0.39	+0.66
Ω/4π (upper limit)	0.32	0.17	0.41	0.13	0.24	0.09	0.19	0.34	0.60
Fe II model[g]: τ_{des}, v_t(km s^{-1})	1.5,3.4	0.5,1.6	0.0,20.	1.0,3.4[f]	0.0,3.4	2.0,3.4	1.0,3.4	0.0,20.	0.0,1.6[f]
Bac model[g]: τ, T_4 (K)	1.0,1.2	0.0,1.0	0.3,1.3	1.0,1.0	0.0,1.0	2.0,1.0	1.0,1.0	1.0,1.0	0.0,1.2

[a] All ultraviolet lines were observed simultaneously with those in the optical, except for 3C 273, for which the *IUE* spectrum from Ulrich *et al.* (1980) was measured.

[b] Uncertainties in line measurements are designated by letters alongside measured values: a = ∼5%, b = ∼10%, c = ∼20%, and d = ∼30%. Colons and double colons indicate large and very large uncertainties.

[c] Hα line measurements for 0405−123 and 0742+318 were taken from Neugebauer *et al.* (1979) and corrected for the appropriate extinction.

[d] He II λ4686 in 1104+167 coincides with atmospheric A band absorption, so this measurement is less reliable than the others.

[e] Equivalent widths are in angstroms in the rest frame and relative to the power-law continuum only. The units of $I(H\beta)$ are 10^{-14} ergs s^{-1} cm^{-2}.

[f] These two models used an iron abundance 3 times that of the standard model.

[g] The photoionization models assume a symmetrical distribution of clouds with no shadowing. Under these conditions, τ_{des} (Balmer continuum optical depth for destruction of Fe II photons) and τ (the optical depth at the Balmer edge describing the Balmer continuum emission) should be the same. Here the Fe II and Balmer continuum models are fitted independently, so τ_{des} and τ can be different purely as a result of the fitting procedure. Note that it is difficult to distinguish observationally between a low τ–high T_4 and a high τ–low T_4 Balmer continuum, over the range of wavelengths of the present fits (see text).

the lines and Balmer continuum, i.e., the spectrum after subtracting the power law shown in Figure 3. The results of fitting models to these spectra are shown in Figures 3*d* and 3*g*, and further information on the fit is given in Table 1.

To summarize, we list all important uncertainties in the fitting procedure: (1) There are uncertainties in the definition of the power law. (2) The underlying continuum may not be a simple power law. Note that nearly all spectra in Figure 3 (*second panel*) diverge from the model approximately beyond Hβ. This excess is confirmed by the infrared data. In the case of 1831+731, where a probable galaxy component is visible on the plates of the National Geographic Society–Palomar Observatory Sky Survey, when the nucleus was fainter, some of the excess may be attributed to the underlying galaxy. (3) An observational calibration uncertainty of 3% corresponds to a 10–15% uncertainty in the power-law–subtracted spectrum. This will not affect the existence of individual features present over scales <200 Å, but may affect the determination of the overall shape of the blended Fe II emission and Balmer continuum, over scales of a few hundred angstroms. (4) An increase in Balmer optical depth can, to some extent, be offset by a decrease in Balmer continuum temperature. (5) It is quite likely that dust extinction, either associated with the BLR or outside it, has modified the line and/or continuum spectrum.

V. DISCUSSION

The matching of the models to our high-quality spectrophotometry yields new information about line and continuum emission in QSOs. Before discussing the consequences of our fits, we note that one crucial problem, that of the importance of intrinsic extinction, is still unresolved (Netzer and Davidson 1979; Kwan and Krolik 1981; MacAlpine 1981; Netzer 1982; Grandi 1983; Lawrence and Elvis 1982).

a) Balmer Continuum and Covering Factor

Our Balmer continuum measurements give a mean ratio $I(\text{Bac})/I(\text{H}\beta) \approx 8$. They are not very different from those found by Malkan and Sargent (1982), Malkan (1983), and Oke, Shields, and Korycansky (1984). However, we believe that our values for the total strength and our estimated shape of this feature are rather better justified as a result of the Fe II and Balmer continuum modeling. The uncertainties, although large, are better understood in physical terms. The total observed Balmer continuum flux is too large by a factor of ≥ 2, when compared with very optically thick models (Fig. 1). The optically thin [$\tau(\text{Bac}) \ll 1$] models have relatively high effective Balmer continuum temperature, and give much better agreement with observation, but they still fail to produce the observed Hα/Hβ intensity ratio. There are several possible ways to explain the discrepancy between the observed and the calculated Balmer continuum. Kwan (1984) has suggested that high densities ($N_e > 10^{10}$ cm^{-3}) can produce large $I(\text{Bac})/I(\text{H}\beta)$. We have tested this by running several high-density models (see below). We find that a strong Balmer continuum is produced only in cases where the X-ray flux is large compared with the ultraviolet ionizing flux. Only in such cases is the transition-zone temperature large enough for collisional ionization from $n \geq 3$ to be efficient. As mentioned already, the Kwan (1984) ionizing continuum is not consistent with the observed X-ray/optical continuum of most QSOs.

Oke, Shields, and Korycansky (1984) have considered the possibility of a large gamma-ray flux producing an extremely deep, warm transition zone. Although gamma-rays have been observed in one or two cases, it is quite clear from general arguments (Netzer 1983) that gamma-rays are not very important. There are other difficulties with this suggestion, mainly the strong predicted, yet unobserved, Paschen continuum. Ionization due to Fe II absorption can explain part of the discrepancy (see below). We should add that the observed Balmer continuum may be produced not only by the emission-line clouds but by, for example, a hot disk (e.g., Malkan 1983). The variation of the Balmer line and continuum intensities over a period of time would be a way of investigating this.

Inspection of Figure 1 suggests that the emergent Balmer continuum flux is directly proportional to the ionizing flux. This can be seen by noting that most of the change in $I(\text{Bac})/I(\text{H}\beta)$ is due to the variation of the Hβ flux [compare $I(\text{Bac})$ with $I(\text{H}\beta)/I(\text{H}\beta$ Case B) in Fig. 1]. This is expected under Case B conditions, but our calculations show that it is also true in QSO clouds. The reason is that for each ionization there is a certain probability of producing a Balmer continuum photon. For $\tau(\text{Bac}) < 1$ most of these photons will escape without interacting further with the gas. The Balmer continuum strength is therefore a good indicator of the cloud covering factor. Similar arguments have been used before for Lyα or Hβ, but the emergent flux in these lines can be rather different from the Case B value, and the covering factor deduced is model-dependent.

Consider a two-component nonthermal power-law continuum with spectral index α_1 at $\lambda < 912$ Å and spectral index α_2 at $\lambda > 912$ Å. The ratio of the flux in the Balmer continuum to the nonthermal flux, measured at the Balmer edge, is

$$F_\nu(\text{Bac})/F_\nu(\text{continuum}) = 1.38 T_4^{-0.65}(\Omega/4\pi) \times [1 - (\nu_{\text{cut}}/\nu_{912})^{-\alpha_1}]/(\alpha_1 4^{\alpha_2}) \quad (9)$$

for $\alpha_1 \neq 0$ and where ν_{cut} is the cutoff frequency of the nonthermal continuum. This expression can be used to estimate the covering factor $\Omega/4\pi$ from the measurement of F_ν(Bac) and F_ν(continuum). Collisional ionization and other processes would increase the Balmer continuum flux (as seems to be the case for most of our objects), so equation (9) gives an upper limit to the covering factor. Obvious uncertainties here are the unknown α_1 (α_2 is measurable; see Table 1) and T_4, which is an average over many zones.

The upper limits for the covering factors deduced from our observations with the assumption of $\alpha_1 = 0.5$ and $\nu_{\text{cut}} = 20$ rydbergs are listed in Table 1. They are all consistent with a small covering factor. Oke, Shields, and Korycansky (1984) give measurements for $F_\nu(\text{Bac})/F_\nu$(continuum) for 29 QSOs. Using equation (9) with $T_4 = 1.5$, we get an average upper limit of 0.25 to the covering factor for their sample. We can also use this method on other objects, in particular, NGC 4151, where Ferland and Mushotzky (1982) suggest a covering factor of ~ 1. From our data for this object we find $\Omega/4\pi \leq 0.15$–0.4, depending on the epoch of observation. The large observed X-ray column density for this source, which was used by Ferland and Mushotzky (1982) to deduce the large covering factor, could be due to a special geometry (e.g., a flat system seen edge-on).

Finally, we should comment on the Balmer continuum shape. Our spectrum fitting shows that all objects can be fitted by either a small-optical-depth, high-temperature continuum or a $T_4 \sim 1.0$, $\tau(\text{Bac}) \sim 1$–2 continuum. It is difficult to distinguish observationally between these two. We note, however, that most photoionization calculations indicate a large contribution to the Balmer continuum from the H^+ zone, which would indicate higher temperatures. Also, our large-optical-depth models tend to underestimate the strengths of the high-order Balmer lines (Fig. 3). The lower order Balmer lines are also underestimated; the observed intensities relative to Hβ, for all our QSOs, are ~ 0.37, ~ 0.20, and ~ 0.12 for Hγ, Hδ, and H7 (compare Table 1 and Fig. 1). We cannot reach a definite conclusion until we resolve the problem of the excess Balmer continuum flux.

b) Fe II Lines

Our model calculations are very successful in fitting almost all the observed Fe II features over the range 1600–5500 Å. In particular, several strong emission features near 3200 Å are positively identified as Fe II lines. We also note the large Fe II contribution near Hγ and Hδ, which must be taken into account when measuring the intensities of these lines. The strong emission feature near 2080 Å (e.g., Wills, Netzer, and Wills 1980; Phillips and Hawley 1978) still presents some difficulties. We cannot decide whether the models produce too little energy at that wavelength or *too much* energy near 2200 Å. This is not surprising in view of the large number of lines considered, and all the uncertainties of the models.

Of much interest are the relative strengths of the optical and ultraviolet Fe II lines. In our sample $4 \leq I[\text{Fe II(UV)}]/[\text{Fe II(opt)}] \leq 12$. If reddening is important, the intrinsic ratio can be twice as large. An immediate conclusion is that all QSOs (and Seyfert 1 galaxies) have strong ultraviolet Fe II lines whether or not the optical Fe II is strong (Wills *et al.* 1980). Even the weakest optical Fe II emitters in our sample have strong ultraviolet Fe II lines.[8] Fe^+ is apparently present even when Fe II(opt) is not detected; therefore we can exclude

[8] This conclusion should be tempered by the fact that the prominence of Fe II features depends on broad-line width.

Ferland and Mushotzky's (1984) suggestion that fast particles in strong radio sources ionize Fe^+ in the transition zone, resulting in no Fe II emission.

As already stressed in Paper I, we find that the main factors determining the relative strengths in the two wavelength bands are the Fe II line optical depths and the Balmer opacity. Our model calculations are quite successful in producing the full observed range of I[Fe II(UV)]/I[Fe II(opt)]. The smallest observed intensity ratio, I[Fe II(UV)]/I[Fe II(opt)] ≤ 4, requires a substantial Balmer optical depth (≥ 1). It is conceivable that some Seyfert galaxies have even smaller I[Fe II(UV)]/I[Fe II(opt)], which will require even larger Balmer opacity. Unfortunately, Fe II lines are sensitive to both τ(Bac) and τ(2343), and the latter is rather uncertain given the large possible range in ionizing radiation and turbulent velocity. Very little or no Balmer opacity is required if reddening is assumed.

The integrated Fe II flux found here is the most important result, and perhaps the most unexpected. If there is no reddening, then, in our sample, the Fe^+ emits more than half the flux of all other lines combined. This can be seen from Table 1, and by considering a typical QSO spectrum where

$$I(\text{C IV } \lambda1549 + \text{C III}] \lambda1909 + \text{Mg II } \lambda2798 + \text{O VI } \lambda1034 + \text{N V } \lambda1240 + \text{O IV } \lambda1402 + \text{He II } \lambda1640 + \text{O III}] \lambda1663 + \text{Balmer lines})/I(\text{Ly}\alpha) = 1.7.$$

The total flux in the Fe II lines is even greater than that of Lyα. There is definitely an "Fe II/Lyα problem." None of the models in Figure 1 produces such strong Fe II lines. The maximum I(Fe II)/I(Lyα) that is still consistent with the relative strengths of other lines is about 0.25. Of course, we might have overlooked an important excitation process for these lines, but, if not, we must consider alternative explanations. Fe II line emission increases relative to other lines in the limit of one or more of the following: high densities, large column densities, low ionization parameter, and high iron abundance. A low ionization parameter results in more intense emission from the transition zone, including Fe II lines. The other strong lines in the transition zone, Lyα, Mg II λ2798, and Hα, are collisionally de-excited in the case of high density and large optical depth. Very high density also helps to reduce the intensity of C II] λ2326.

We have considered in detail several cases that favor the emission of Fe II lines over that of other ions. Sample results are shown in Table 2. The continuum assumed is the same as before except that the cutoff frequency is at 5 rydbergs. This increases the relative importance of ionization by X-ray photons. The results confirm that extremely intense Fe II lines can indeed be emitted under some circumstances. Model 3 is quite satisfactory in producing the observed I(Fe II)/I(Lyα), I(Fe II)/I(C II] λ2326), and I(Fe II)/I(Mg II λ2798) in the more extreme objects. However, it does not produce the observed strengths of the high-excitation lines, such as C IV λ1549, and intercombination lines such as C III] λ1909. Such a model could explain only part of the observed spectrum, and another component of higher ionization parameter and lower densities must be added.

The idea that the emission regions of QSOs cannot be produced by a single ionization parameter is not new. Netzer (1976) has suggested a spherical geometry with a volume-averaged ionization parameter as a possible model. Davidson (1977) has considered in detail two-component models where optically thin clouds produce the observed strong O VI and N V lines. Baldwin and Netzer (1978) have further investigated this idea. The case considered here is rather different—two optically thick components, with different ionization parameter and density. The high ionization parameter component produces little Lyα, some Balmer lines, and all the highly excited metallic lines. The high-density material produces only low-excitation lines, mainly of Fe II and hydrogen. Collin-Souffrin, Dumont, and Tully (1982) have considered a similar idea, but in their model, heating and ionization of the high-density component is not by photoionization. The physical conditions in their high-density clouds are rather different from the low-temperature, photoionized gas considered here.

There are several difficulties associated with the idea of high-density clouds. Most important, the gas pressure of the high-density material is more than an order of magnitude larger

TABLE 2

HIGH-DENSITY MODELS[a]

	Model 1	Model 2	Model 3
U_1 (cm s^{-1})	3.8×10^8	3.8×10^7	3.8×10^7
N_H (cm^{-3})	10^{10}	10^{11}	10^{11}
τ_{912}	10^7	10^7	10^7
Fe abundance	3	1	3
I(Lyα)	14	7.7	8.1
I(Hα)	4.8	3.4	3.4
I(Hβ)	1	1	1
I(Paα)	0.43	0.32	0.33
I(C IV λ1549)	8.9	0.9	0.9
I(C III] λ1909)	1.2	0.13	0.13
I[Fe II(total)]	8.3	5.0	8.2
I[Fe II(UV)]/I[Fe II(opt)]	1.90	1.80	1.85
I(Mg II λ2798)	0.9	1.7	1.3
I(C II] λ2326)	0.85	0.35	0.24
I(Bac)	2.3	3.1	3.1

[a] The ionizing continuum has two components: (1) $F_\nu \approx \nu^{-0.5} \exp(-\nu/5$ rydbergs), and (2) an X-ray component with $F_\nu \approx \nu^{-0.7}$. We use a constant-gas-pressure model with N_H the hydrogen density at the illuminated face. See the text for the definition of U_1. In models 1 and 3 we assume cosmic abundances, except for iron, where the enhancement over the cosmic value is given.

than that in the lower density clouds. If some hot confining medium is assumed, then the two kinds of clouds must be associated with two distinct regions. Cloud motion and line profiles are other important considerations, and so is the problem of cloud stability.

We should add that the models in Table 2 have very low temperatures (5000–6500 K) in the main Fe II emission zones. Models with the Kwan and Krolik (1981) continuum have higher temperature and require smaller τ_{912} to give $I(\text{Fe II})/I(\text{Ly}\alpha) = 1$.

The situation is very different if dust is present in the source but outside the broad-line region. For example, if $A_V \approx 0.6$ mag, then, using a λ^{-1} extinction law, typical intrinsic line ratios would be $I(\text{Ly}\alpha)/I(\text{H}\beta) = 50$, $I(\text{Fe II})/I(\text{Ly}\alpha) \sim 0.3$. Several cases can produce these line ratios, including those shown in Figure 1, but with increased Fe II abundance. In these cases a single ionization parameter model gives better agreement with most observed lines, including Fe II.

The large flux of the ultraviolet Fe II lines has important consequences for conditions in the transition zone. In particular, ionization of hydrogen resulting from absorption of Fe II and Mg II lines can determine the electron density and neutral fraction at the back side of the cloud. Each ionization of $n = 2$ by absorption of an Fe II photon produces about 0.3 new Balmer photons, each with about 80% of the energy of the ionizing photon. Thus the Balmer flux due to this process is about 25% of the flux of the Fe II photons destroyed. In several of the models that we have calculated, about half the Fe II photons that are produced in the cloud ionize hydrogen. These models underestimate the observed Fe II flux, but by using the observed $I(\text{Fe II})/I(\text{H}\beta)$ we can explain a large fraction of the observed Balmer continuum and the reason why the value of $I(\text{Bac})/I(\text{H}\beta)$ in Figure 1 is too small. Balmer lines are also affected, and the covering factor deduced would be considerably smaller than the limit obtained using equation (9).

c) *Iron Abundance*

The models shown in Figure 1 predict $1.5 \leq I[\text{Fe II(tot)}]/I(\text{Mg II } \lambda 2798) \leq 4$. Similar ratios are predicted by models with different ionizing continua. We observe much stronger Fe II lines, typically $I[\text{Fe II(tot)}]/I(\text{Mg II } \lambda 2798) \sim 8$. None of the cosmic-abundance models tried produces such a large line ratio. Also, as seen in Table 2, differences due to Balmer opacity or gas density cannot result in such a large ratio. If no important excitation processes have been neglected, we are led to conclude that iron overabundance by a factor of ~ 3 is a likely explanation. This refers mainly to the Fe/Mg abundance ratio, but the total strength of Fe II lines suggests that overabundance relative to hydrogen is a possibility. The increase in the total strength of Fe II lines is not directly proportional to the increase in iron abundance, since strong Fe II models have lower temperatures [$\tau(2343)$ is directly proportional to the iron abundance].

If iron is indeed overabundant in QSOs and active galaxies, this may have important implications for their evolution. Type I supernovae show indications of iron enrichment (see Branch *et al.* 1983), but it is difficult to think of a way in which QSOs would experience a large production of such objects. More generally, stars with masses in the range 3–7 $M_\odot$ may be responsible for much of the iron production in the universe (Shklovskii 1984), suggesting special stellar evolution in QSOs.

d) Fe I *Lines*

Several objects that we have fitted show a flux excess at wavelengths corresponding to those of strong Fe I multiplets, although in Paper I we have already noted that many lines previously thought to be Fe I are in fact due to Fe II. We did not attempt detailed modeling of the Fe I atom, but note that two of the more intense multiplets, those at 3860 and 3710 Å, are predicted to emit about 5% of the intensity of Fe II in some models. This is higher than observed, and this problem should be further investigated.

Some of our *IUE* results used here will be published in detail later. M. A. J. Snijders kindly supplied the *IUE* spectrum of 3C 273, originally published by Ulrich *et al.* (1980). Our QSO continuum observations also involve photometry by D. Lester and one of us (B. J. W.) at the Infrared Telescope Facility (IRTF), and *UBVRI* photometry by W. Wiśniewski at the LPL Mount Lemmon Observatory. We thank these people, including the staffs of the *IUE* and *IRTF* observatories. We appreciate the work of the staff at McDonald Observatory, especially that of D. R. Doss, for maintaining the IDS spectrograph and other instruments. Invaluable tape-reading help was given by F. A. Bozyan and L. E. Smith (University of Texas Physics Department). We are grateful to C. M. Gaskell for discussions and many helpful comments on the manuscript and to E. S. Barker for the use of his extinction coefficient and air-mass programs. H. N. thanks H. J. Smith and F. N. Bash for hospitality in the University of Texas Astronomy Department, while on sabbatical leave from Tel-Aviv University. We thank the NSF for support through grants AST-7815916, AST-7901182, and AST-8215477, the US–Israel Binational Science Foundation for support through grant 2305/80, and NASA for support through grants NSG 5387 and NAG 5-258.

APPENDIX

THE SPECTROGRAPH, OBSERVATIONS, AND REDUCTIONS

The observations were obtained with the UVITS spectrograph and IDS detector at the f/9 Cassegrain focus of the McDonald Observatory 2.7 m reflector. A Quantex television system (S20 photocathode) is used for finding and guiding. In the finding field of $3' \times 5'$, the magnitude limit is 21 mag in typical seeing conditions. The spectrograph, originally designed by W. A. Hiltner, was modified by G. Chincarini and later adapted for use with the IDS detector by P. M. Rybski (Rybski, Mitchell, and Montemayor 1977). An adjustable reflective decker above a unilateral slit jaw defines two entrance apertures, of east-west separation 51″ projected on the sky. The off-axis collimator is matched to the f/9 telescope beam (with a focal-plane scale of 8.″625/mm). The dispersing element is one of three 600 line mm^{-1} diffraction gratings blazed near 4000, 5000, and 7500 Å. The slit is then imaged on the detector by a f/1.4 folded Cassegrain Schmidt camera with

quartz corrector plate, giving two spectra 28 mm (~3000 Å) long and separated by 1 mm. After a quartz field flattener, the IDS detector system employs one of two three-stage image-tube chains with ultraviolet transmitting fiber optics faceplate and with fiber optics and oil coupling between image tubes and the dissector scanner. One chain is used from the atmospheric cutoff to about 6500 Å (first-stage image tube ITT F4051) and the other from 3700 to 8700 Å (first-stage image tube Varo 8605/1 "UV"). The dissector aperture is 26 × 255 μm (width × length), and its length determines the maximum slit length that can be safely used for spectrophotometry (~6″.7). The wavelength resolution is about 6.5 Å (FWHM) using a narrow slit, and up to 12 Å (depending on the seeing image size) with the largest slit width used for the present observations (6″.7). The maximum efficiency of the telescope-spectrograph-detector system is about 5%

Although the McDonald IDS is similar to the Lick Observatory dissector scanner described by Robinson and Wampler (1972), its improved electron optics results in improved resolution and much reduced width of line wings to which the earlier systems were subject. A rotation of the electron image (but not the image on the phosphor) as the telescope tracks is thought to be caused by interaction of the beam with the Earth's magnetic field. This is taken out in software every 20 min by rotation of the "ramps," the computed x-y coordinates traced by the electron beam as it scans the output phosphor of the final image-tube stage. The dissector scans the two spectra at 250 Hz, and the data are accumulated in two arrays of 2048 pixels each. Thus the spectra are oversampled by more than a factor of 2. The object is moved in an ABBA cycle between the apertures A and B of the spectrograph by computer-controlled movement of the telescope. Data are recorded after integration in each aperture. For the present observations this integration time was about 50 s.

An important property of the detector dictates some aspects of our observing technique. The finite phosphor decay time, which allows the 4096 pixels to be scanned in a time interval as long as 4 ms, results in a faint but significant residual image, detectable from bright stars even after 1 hour. For a constant input signal the output of the phosphor increases as a function of time, rapidly in the first few seconds, then by only 10% over the next few minutes. The output signal growth and decay are apparently dependent on the exposure history of the phosphor (Rybski 1980). These complications are largely avoided by the background-subtraction (ABBA) observing technique, provided that the integration times and cycle times are kept the same for the standard stars and program objects, so for spectrophotometric observations exposures are made in the B and then the A apertures before data recording, to mimic the "BA" end of the "ABBA" sequence in order to avoid the effect of the rapid initial rise in phosphor response to a strong input signal. Tests with standard stars or with a constant light source show an increase of about 2–3% in background-subtracted signal between the first and second recorded ABBA cycles, but constant values thereafter. Tests with a quartz halide lamp (see below), opening and closing the camera shutter to mimic ABBA cycles and repeating the observations with a neutral density filter in the light path, showed the system to be linear to within 2% over the 5 mag range corresponding to the signals encountered in observing the standard stars and QSOs of the present program. We also tested the dependence of output signal on the level of background phosphor glow for a quartz-lamp signal corresponding to that from a 15 mag QSO. The output signal was 3.5% higher for 2–3 min after exposing the detector to a strong lamp signal–certainly much stronger than would apply to real observations. Real observations are not made immediately after exposure to a strong signal, so we have ignored this effect.

For removal of pixel-to-pixel sensitivity variations we observe a quartz halide ("flat-field") lamp that illuminates the spectrograph aperture after diffuse reflection from the back of the TV field-viewing mirror. Although this light does not follow exactly the same optical path as an astronomical "point" source, experience shows that irregularities in response across the tubes can usually be corrected to much better than 2–3% of the total signal. Flat-field lamp exposures are made at the beginning and end of a night's observations.

The wavelength comparison lamps (Westinghouse hollow-cathode iron-neon and iron-argon) were observed after each complete observation (of a QSO or a standard star), generally with the telescope at the mean hour angle of the preceding observation. The dispersion curves (fifth-order polynomials) determined for narrow-slit observations apply well to the data, except for about 50 channels at the short-wavelength end of the red-chain spectra. There are also small shifts, significant only in the direction of dispersion. For long integrations (e.g., 2 hours) the FWHM can be increased from 7.5 to 8 Å. These small shifts can be checked either from known wavelengths of narrow lines in astronomical spectra or by night-sky lines, if one of the few airglow lines visible from McDonald (O I λ5577, Na I λ5892, or O I λλ6300, 6364) is within the observed wavelength range (the "red" setting only). In addition to the above uncertainties, dispersion curves for observations with wide slits (usually 5″ to 6″.7) are uncertain because the path of the object light through the spectrograph is determined by the position of the image in the aperture. This is wavelength-dependent for observations where atmospheric refraction is significant (a shift of 2 Å between 3600 and 5500 Å at a zenith distance of 45°).

Small- and large-slit observations were made at as small an air mass as practicable, within constraints imposed by weather, declination, and availability of suitable flux standard stars (usually from Stone 1977, and occasionally from Oke 1974). Standards were observed as close as possible to QSOs, in time and sky position and/or air mass, in order to minimize uncertainties due to light loss as a result of seeing and differential refraction, and variations of air mass with time and position—especially important in regions of strong atmospheric absorption (H_2O, OH bands), and in the ultraviolet (O_3). Typically, 3–4 standard stars are observed each night. For large-aperture observations and sometimes for small-aperture observations the QSO was centered by maximizing the signal through the spectrograph aperture. The accuracy of centering is probably a small but significant source of uncertainty in poor seeing and/or where observations had to be made at larger air mass.

In order to cover the range from 3200 to 8700 Å, spectra are combined from three different detector chain and grating configurations. Typical useful wavelength ranges were 3200–5600 Å, 4000–7000 Å, and 6000–8700 Å. Note that the maximum wavelength range of 3000 Å was not always used. This was because the extreme ultraviolet and red light, already reduced by atmospheric absorption and decreasing photocathode and grating efficiency, would have been further reduced by vignetting (up to a factor of 2 at the extreme ends of the spectrum).

Individual ~50 s integrations are recorded on magnetic tape. The reduction procedure consists of first applying small dead-

time corrections (usually negligible, but up to 10% in some wavelength ranges for the brightest standard stars, when using large apertures), then comparing the shapes of separate spectra with the average to remove the rare "spikes," about 4–5 channels wide, which are thought to be due to electrical breakdown between the cathode and image-tube housing. (Their frequency is minimized by passing a mixture of dry nitrogen and freon over the front window of the image-tube chain.) This same program gives a listing of the total "signal" for each ABBA cycle, as a check on the photometric quality of the data. The subsequent co-addition, sky-subtraction, calibration, and so on is quite standard (Uomoto 1981). Mean atmospheric extinction coefficients appropriate to McDonald Observatory are applied to standard stars and QSOs. For calibration of spectra that included data near the atmospheric cutoff around 3200 Å, a dust, ozone, and Rayleigh scattering model appropriate for the altitude of McDonald (2075 m) was used to determine seasonal (bimonthly mean) extinction coefficients (Allen 1973). Except for $\lambda < 3300$ Å, uncertainties in the final spectra as a result of these corrections are negligible.

The calibration program allows division of standard stars and QSO data by any flat-field spectrum to remove pixel-to-pixel gain variations. These divided spectra are retained without normalization throughout the calibration procedure. Thus we are able to divide the QSO spectra by spectra of hot stars to remove A, a, B and other atmospheric absorption features, or to use spectra of hot stars as flat-field spectra in regions <3500 Å where the signal from the quartz lamp is low. Calibration between 3100 and 3500 Å was usually checked by running the data of a nearby standard star through the same calibration procedure as that for a program QSO spectrum.

The present program has two requirements that have been met by nearly all spectra used in this study. First, in order to determine the shapes of blended features, often just a few percent of the continuum, high signal-to-noise ratios are needed. Many of our final spectra are the sum of several, obtained on different nights and with slightly different grating settings, thus minimizing any systematic effects present in individual spectra. The spectra sometimes required small (<1 Å) shifts to align spectral features, and only those spectra showing no evidence for real time variability, as judged by equivalent widths of the emission lines, were included. Spectra were weighted in proportion to the inverse square of the noise as measured in wavelength regions relatively free of spectral features. The noise is a function of wavelength, so spectra observed with different grating settings required different weights for different wavelength regions. A useful measure of the relative signal-to-noise ratio of two spectra, in regions where there were many emission features, was obtained by dividing each by a third spectrum. For some spectra and in some wavelength regions the signal-to-noise ratio exceeds 200. The second requirement of the program was careful calibration of the spectral shape over the 3200–8500 Å wavelength range. Thus the overall shapes of the high signal-to-noise ratio co-added spectra were normalized to those spectra obtained with the largest apertures under photometric sky conditions. Except near 3200 Å, the relative calibration is thought to be accurate to 5–10% up to 7200 Å. The very red (to 8500 Å) spectra have larger calibration uncertainties because (1) smaller apertures were used to reduce the effects of large and variable atmospheric water-vapor and OH emission bands, (2) numerous atmospheric absorption bands become more difficult to correct, and (3) (not unrelated to item 2) the uncertainties in the flux densities of the standard stars are larger. It is possible that some very red spectra could be in error by as much as 20% near 8500 Å. Because spectra in different wavelength regions overlap by ≥ 1000 Å, the relative calibrations could be compared. Often spectra were poorly calibrated at the ends (100–200 Å), but since these overlap with a well-calibrated region of an adjacent spectrum, small corrections could be made at the ends. The blue, red, and very red spectra were co-added, using relative weights in the overlap regions as described above.

REFERENCES

Allen, C. W. 1973, *Astrophysical Quantities* (3rd ed.; London: Athlone), p. 126.
Baldwin, J. A., and Netzer, H. 1978, *Ap. J.*, **226**, 1.
Bechtold, J., Green, R. F., Weymann, R. J., Schmidt, M., Estabrook, F. B., Sherman, R. D., Wahlquist, H. D., and Heckman, T. 1984, *Ap. J.*, **281**, 76.
Bergeron, J., and Kunth, D. 1984, *M.N.R.A.S.*, **207**, 263.
Bonilha, J. R. M., Ferch, R., Salpeter, E. E., Slater, G., and Noerdlinger, P. D. 1979, *Ap. J.*, **233**, 649.
Branch, D., Lacy, C. H., McCall, M. L., Sutherland, P. G., Uomoto, A. K., Wheeler, J. C., and Wills, B. J. 1983, *Ap. J.*, **270**, 123.
Brocklehurst, M. 1971, *M.N.R.A.S.*, **153**, 471.
Brown, R. L., and Mathews, W. G. 1970, *Ap. J.*, **160**, 939.
Collin-Souffrin, S., Dumont, S., and Tully, J. 1982, *Astr. Ap.*, **106**, 362.
Davidson, K. 1977, *Ap. J.*, **218**, 20.
Davidson, K., and Netzer, H. 1979, *Rev. Mod. Phys.*, **51**, 715.
Drake, S. A., and Ulrich, R. K. 1980, *Ap. J. Suppl.*, **49**, 545.
Eastman, R. G., MacAlpine, G. M., and Richstone, D. O. 1983, *Ap. J.*, **275**, 53.
Ferland, G. J., and Elitzur, M. 1984, *Ap. J. (Letters)*, **285**, L11.
Ferland, G. J., and Mushotzky, R. F. 1982, *Ap. J.*, **262**, 564.
———. 1984, *Ap. J.*, **286**, 42.
Ferland, G. J., and Netzer, H. 1979, *Ap. J.*, **229**, 274.
Gaskell, C. M. 1981, Ph.D. thesis, University of California, Santa Cruz.
Grandi, S. A. 1981, *Ap. J.*, **251**, 451.
———. 1982, *Ap. J.*, **225**, 25.
———. 1983, *Ap. J.*, **268**, 591.
Green, R. F., Pier, J. R., Schmidt, M., Estabrook, F. B., Lane, A. L., and Wahlquist, H. D. 1980, *Ap. J.*, **239**, 483.
Hubbard, E. N., and Puetter, R. C. 1985, *Ap. J.*, submitted.
Krolik, J. H., and McKee, C. F. 1978, *Ap. J. Suppl.*, **37**, 459.
Kurucz, R. L. 1981, *Smithsonian Ap. Obs. Spec. Rept.*, No. 390.
Kwan, J. 1984, *Ap. J.*, **283**, 70.
Kwan, J., and Krolik, J. H. 1981, *Ap. J.*, **250**, 478.
Lawrence, A., and Elvis, M. 1982, *Ap. J.*, **256**, 410.
Lochte-Holtgreven, W. 1958, *Rept. Progr. Phys.*, **21**, 312.
MacAlpine, G. M. 1981, *Ap. J.*, **251**, 465.
Malkan, M. A. 1983, *Ap. J.*, **268**, 582.
Malkan, M. A., and Sargent, W. L. W. 1982, *Ap. J.*, **254**, 22.
Mathews, W. G. 1982, *Ap. J.*, **252**, 39.
Netzer, H. 1975, *M.N.R.A.S.*, **171**, 395.
———. 1976, *M.N.R.A.S.*, **177**, 473.
———. 1977, *M.N.R.A.S.*, **178**, 489.
———. 1980, *Ap. J.*, **236**, 406.
———. 1982, *M.N.R.A.S.*, **198**, 589.
———. 1983, in *Proc. 24th Liège International Astrophysical Colloquium, Quasars and Gravitational Lenses*, ed. J. P. Swings (Institut d'Astrophysique, Université de Liège), p. 398.
———. 1985, *Ap. J.*, in press.
Netzer, H., and Davidson, K. 1979, *M.N.R.A.S.*, **187**, 871.
Netzer, H., and Ferland, G. J. 1984, *Pub. A.S.P.*, **96**, 593.
Netzer, H., and Wills, B. J. 1983, *Ap. J.*, **275**, 445 (Paper I).
Neugebauer, G., Oke, J. B., Becklin, E. E., and Matthews, K. 1979, *Ap. J.*, **230**, 79.
Oke, J. B. 1974, *Ap. J. Suppl.*, **27**, 21.
Oke, J. B., Shields, G. A., and Korycansky, D. G. 1984, *Ap. J.*, **277**, 64.
Osterbrock, D. E., and Cohen, R. D. 1982, *Ap. J.*, **261**, 64.
Phillips, M. M., and Hawley, S. A. 1978, *Pub. A.S.P.*, **90**, 650.
Puetter, R. C., Burbidge, E. M., Smith, H. E., and Stein, W. A. 1982, *Ap. J.*, **257**, 487.
Puetter, R. C., and Hubbard, E. N. 1983, *Ap. J.*, **273**, 36.
Puetter, R. C., and LeVan, P. D. 1982, *Ap. J.*, **260**, 44.
Robinson, L. B., and Wampler, E. J. 1972, *Pub. A.S.P.*, **84**, 161.
Rybski, P. M. 1980, *Bull. AAS*, **12**, 751.
Rybski, P. M., Mitchell, A. L., and Montemayor, T. 1977, *Pub. A.S.P.*, **89**, 621.
Seaton, M. J. 1964, *M.N.R.A.S.*, **127**, 177.
Shklovskii, I. S. 1984, *J. Ap. Astr.*, **5**, 13.

Stone, R. P. S. 1977, *Ap. J.*, **218**, 767.
Ulrich, M. H., *et al.* 1980, *M.N.R.A.S.*, **192**, 561.
Uomoto, A. K. 1981, University of Texas Department of Astronomy Internal Report: Data Reduction for the Cassegrain Spectrographs.
Wills, B. J., Netzer, H., Uomoto, A. K., and Wills, D. 1980, *Ap. J.*, **237**, 319.
Wills, B. J., Netzer, H., and Wills, D. 1980, *Ap. J.* (*Letters*), **242**, L1.
Wills, B. J., Wills, D., Lester, D., and Netzer, H. 1984, in preparation.
Zamorani, G., *et al.* 1981, *Ap. J.*, **245**, 357.

H. NETZER: Royal Greenwich Observatory, Herstmonceux Castle, Hailsham, Sussex BN27 1RP, England, UK

B. J. WILLS and D. WILLS: Department of Astronomy, RLM 15.308, University of Texas, Austin, TX 78712